Flow, Turbulence and Combustion (2024) 113:481–517
https://doi.org/10.1007/s10494-024-00550-6

RESEARCH

Effects of Pressure and Characteristic Scales on the Structural and Statistical Features of Methane/Air Turbulent Premixed Flames

Jamie Bowers[1] · Eli Durant[1] · Reetesh Ranjan[1]

Received: 28 June 2023 / Accepted: 15 April 2024 / Published online: 4 May 2024

Abstract

In this study, the highly nonlinear and multi-scale flame-turbulence interactions prevalent in turbulent premixed flames are examined by using direct numerical simulation (DNS) datasets to understand the effects of increase in pressure and changes in the characteristic scale ratios at high pressure. Such flames are characterized by length-scale ratio (ratio of integral length scale and laminar thermal flame thickness) and velocity-scale ratio (ratio of turbulence intensity and laminar flame speed). A canonical test configuration corresponding to an initially laminar methane/air lean premixed flame interacting with decaying isotropic turbulence is considered. We consider five cases with the initial Karlovitz number of 18, 37, 126, and 260 to examine the effects of an increase in pressure from 1 to 10 atm with fixed turbulence characteristics and at a fixed Karlovitz number, and the changes to characteristic scale ratios at the pressure of 10 atm. The increase in pressure for fixed turbulence characteristics leads to enhanced flame broadening and wrinkling due to an increase in the range of energetic scales of motion. This further manifests into affecting the spatial and state-space variation of thermo-chemical quantities, single point statistics, and the relationship of heat-release rate to the flame curvature and tangential strain rate. Although these results can be inferred in terms of an increase in Karlovitz number, the effect of an increase in pressure at a fixed Karlovitz number shows differences in the spatial and state-space variations of thermo-chemical quantities and the relationship of the heat release rate with the curvature and tangential strain rate. This is due to a higher turbulent kinetic energy associated with the wide range of scales of motion at atmospheric pressure. In particular, the magnitude of the correlation of the heat release rate with the curvature and the tangential strain rate tend to decrease and increase, respectively, with an increase in pressure. Furthermore, the statistics of the flame-turbulence interactions at high pressure also show sensitivity to the changes in the characteristic length- and velocity-scale ratios. The results from this study highlight the need to accurately account for the effects of pressure and characteristic scales for improved modeling of such flames.

Keywords Turbulent premixed flame · Direct numerical simulation · High pressure · Curvature · Tangential strain-rate · Heat release rate

Extended author information available on the last page of the article

1 Introduction

Turbulent premixed combustion is observed in several applications such as automotive engines, power generation devices, and propulsion devices. Such applications are typically operated at high pressure, under lean conditions, and intense turbulent environments to attain higher efficiency, compact design, and better emissions (Kobayashi et al. 2005; Dunn et al. 2007; Bagdanavicius et al. 2013). The highly nonlinear flame-turbulence interaction prevalent in such applications is a multi-scale phenomenon (Peters 2000; Poinsot and Veynante 2005; Gonzalez-Juez et al. 2017; Driscoll et al. 2020; Steinberg et al. 2021), where the interplay of various processes such as chemical reactions, molecular and turbulent mixing, convective processes, differential diffusion, and thermal expansion occur within the flame region. The presence of such multi-scale processes and their interactions makes the investigation and modeling of such flames a challenging task. At high pressure, the complexity of flame-turbulence interactions is increased further leading to an increased difficulty in their modeling (Daniele et al. 2013). Although there have been several studies in the past to examine the fundamental features of high-pressure turbulent premixed flames (Inauen and Kreutner 2003; Kobayashi et al. 2005; Lachaux et al. 2005; Liu et al. 2012; Wang et al. 2013, 2015; Fragner et al. 2015; Dinesh et al. 2016; Yilmaz and Gokalp 2017; Savard et al. 2017; Wang et al. 2018; Klein et al. 2018; Zhang et al. 2019; Wang et al. 2019a, b; Alqallaf et al. 2019; Lu and Yang 2020), further studies are still needed for an improved understanding of the effects of pressure and characteristic scales associated with the flame and turbulence on such flames to facilitate their reliable and predictive modeling in practical systems (Keppeler et al. 2014).

In turbulent premixed flames, the flame surface gets wrinkled and stretched by eddies of different sizes leading to increased surface area and the burning rate. Therefore, turbulent premixed flames are usually characterized by characteristic length (l/δ_L) and velocity (u'/S_L) scale ratios associated with the turbulence and the flame (Peters 2000). Here, l, δ_L, u', and S_L denote integral length scale, thermal flame thickness, turbulence intensity, and laminar flame speed, respectively. Based on these ratios, the flames are classified to be in different regimes, such as laminar, wrinkled flamelet (WF), corrugated flamelet (CF), thin reaction zone (TRZ), and broken/distributed reaction zone (B/DRZ) regimes. These regimes can also be characterized in terms of non-dimensional numbers, such as Karlovitz number ($Ka = \sqrt{u'^3\delta_L/S_L^3 l}$), Reynolds number ($Re = u'l/\nu$) and Damköhler number ($Da = S_L l/u'\delta_L$), where, ν denotes the kinematic viscosity. A detailed description of the regimes of the premixed flames is provided elsewhere (Peters 2000; Poinsot and Veynante 2005). Here, we summarize some key features of TRZ and B/DRZ regimes, as the flames considered in this study correspond to these regimes.

The TRZ regime is characterized by $1 < Ka < Ka_c$, where $Ka_c \approx 100$. In this regime, the preheat zone gets thickened by the eddies, but the reaction zone remains unaffected as the small-size eddies get dissipated before they can disrupt the reaction zone (Trouve and Poinsot 1994). Some other features of this regime include increased wrinkling of the flame surface, enhanced heat and mass transport within the flame brush, and an increase in fuel consumption compared to the unstretched laminar flame. In the B/DRZ regime ($Ka > Ka_c$), the transport by energetic turbulent eddies dominates differential diffusion, and therefore, can potentially lead to local/global extinction (Peters 2000). Some of the experimental and numerical studies of such flames have shown that local extinction can occur for $Ka \gg Ka_c$ due to gas expansion across the flame region (Mansour et al. 1998; Dunn et al. 2007; Aspden et al. 2011; Savre et al. 2013; Lapointe et al. 2015). Flames in this regime also exhibit a diffused interface between fuel and products with the flame structure resembling a turbulent mixing zone. Past studies of methane/air flames in TRZ and B/DRZ regimes have also shown a progressive broadening of the flame brush with an increase in u'/S_L (Mansour et al. 1998; De Goey et al. 2005; Dunn et al. 2007, 2009; Wabel et al. 2017; Zhou et al. 2017). These studies have shown that the flame-turbulence interactions in the premixed flames within these regimes are significantly affected by the characteristic scales associated with the flame and turbulence i.e., u'/S_L and l/δ_L. The present study focuses on examining the effects of changes to u'/S_L or/and l/δ_L at high pressure.

Past studies have examined several features of high-pressure turbulent premixed flames (Inauen and Kreutner 2003; Kobayashi et al. 2005; Lachaux et al. 2005; Dinkelacker et al. 2011; Liu et al. 2012; Wang et al. 2013; Yenerdag et al. 2015; Wang et al. 2015; Fragner et al. 2015; Ratzke et al. 2015; Dinesh et al. 2016; Yilmaz and Gokalp 2017; Savard et al. 2017; Wang et al. 2018; Klein et al. 2018; Zhang et al. 2019; Wang et al. 2019a, b; Alqallaf et al. 2019; Lu and Yang 2020; Rieth et al. 2023). These studies have considered different configurations (planar, Bunsen, spherical, slot, bluff-body), different fuels (methane, propane, hydrogen, syngas, ammonia, etc.), different regimes (CF, WF, and TRZ), and a range of pressure (up to $\mathcal{O}(100)$ atm). The outcomes of these studies have shown that compared to the corresponding atmospheric pressure flames, high-pressure flames exhibit an enhanced small-scale wrinkling, which manifests into an enhanced flame surface density (FSD) and burning rates; a higher probability of higher magnitude of curvature, and increased skewness of its probability density function (PDF); a significant increase in the heat release rate; a decrease in the de-correlation of heat release with the fuel consumption rate; a significant variation of S_T/S_L where S_T is the turbulent flame speed; a prevalence of small-scale (higher wavenumbers) flame structures; and inaccuracies associated with a fast chemistry assumption. Most of the past studies have been experimental with a limited number of numerical investigations (Fragner et al. 2015; Yilmaz and Gokalp 2017; Savard et al. 2017; Wang et al. 2018, 2019a, b) of high-pressure turbulent premixed flames. Therefore, there is a need for further understanding of flame-turbulence interactions at high pressure under different operating conditions, which will contribute to the existing understanding to facilitate predictive and reliable modeling of such flames in practical applications.

In recent years, due to advancements in computational resources, there have been a growing number of studies where direct numerical simulation (DNS) is used as a computational tool to investigate the fundamental features of turbulent premixed flames in different geometries, regimes, and approaches of handling chemical kinetics (Chen 2011; Driscoll et al. 2020; Steinberg et al. 2021). In DNS, all the relevant spatial and temporal scales are resolved adequately by the employed grid, and accurate numerical methods are used to perform the computations. Such studies facilitate the assessment and development of accurate and efficient models, which in turn can be used to study practical applications. Therefore, similar to some of the past computational studies of high-pressure turbulent premixed flames (Fragner et al. 2015; Yilmaz and Gokalp 2017; Wang et al. 2018, 2019a, b; Rieth et al. 2023), we employ a DNS-based strategy to examine the features of such flames. Note that DNS of a high-pressure flame is computationally more challenging compared to an atmospheric pressure flame under the same background turbulence characteristics (u' and l) due to a decrease in δ_L and ν, which increases the grid resolution requirements for accurately representing spatio-temporal features of both flame and turbulence.

In the present study, we consider a canonical turbulent premixed configuration where an initially laminar methane/air lean premixed flame interacts with decaying isotropic turbulence. We perform DNS of five cases by employing moderately complex finite-rate chemical kinetics. The key objective of this study is to assess the effects of an increase in pressure from 1 to 10 atm for fixed values of u' and l and at a fixed value of Ka, and to examine the effects of changes in u'/S_L and l/δ_L at the pressure of 10 atm for fixed values of l/δ_L, and u'/S_L, respectively, on the features of flame-turbulence interactions. Based on the initial conditions, two cases correspond to the TRZ regime, one case corresponds to the B/DRZ regime, and two cases correspond to the boundary of the TRZ and B/DRZ regimes. The structural features of the flame-turbulence interactions are analyzed in terms of flame brush, vorticity, global flame metrics, kinetic energy spectrum, and spatially averaged thermo-chemical quantities. The statistical features of flames are examined in terms of state-space variation and single-point statistics of several thermo-chemical quantities that characterize flame-turbulence interactions. A particular focus of the study is on understanding the relationship of heat release rate with the curvature and tangential strain rate on the flame surface, which are key quantities from the modeling perspective (Echekki and Chen 1996; Tanahashi et al. 2000; Chakraborty and Cant 2004). The past studies have not examined this aspect in detail for high-pressure methane/air turbulent premixed flames. The detailed analysis of the flames considered in this study will apart from providing an improved understanding of such flames, will also lead to reference datasets and results for future model development and assessment studies.

This article is arranged as follows. The mathematical formulation and numerical methodology are described in Sect. 2. The description of the computational setup is presented in Sect. 3. The results from this study are discussed in Sect. 4. Finally, the outcomes of the present study are summarized in Sect. 5.

2 Mathematical Formulation and Numerical Methodology

In this section, we first describe the governing equations. Afterward, a brief description of the employed numerical methodology is discussed.

2.1 Governing Equations

We consider a fully compressible formulation with finite-rate chemistry effects to examine the flame-turbulence interactions in turbulent premixed flames. The governing equations comprise the compressible multi-species reacting Navier–Stokes equations, which correspond to the conservation of mass, momentum, energy, and species mass. These equations are given by

$$\frac{\partial \rho}{\partial t} + \frac{\partial \rho u_i}{\partial x_i} = 0, \tag{2.1}$$

$$\frac{\partial \rho u_i}{\partial t} + \frac{\partial}{\partial x_j}\left[\rho u_i u_j + p\delta_{ij} - \tau_{ij}\right] = 0, \tag{2.2}$$

$$\frac{\partial \rho E}{\partial t} + \frac{\partial}{\partial x_i}\left[(\rho E + p)u_i + q_i - u_j\tau_{ij}\right] = 0, \tag{2.3}$$

$$\frac{\partial \rho Y_k}{\partial t} + \frac{\partial}{\partial x_i}\left[\rho Y_k\left(u_i + V_{k,i}\right)\right] = \dot{\omega}_k, \qquad k = 1, ..., N_s. \tag{2.4}$$

Here, ρ is the density, $(u_i)_{i=1,2,3}$ is the velocity component in the Cartesian coordinates, E is the specific total energy, and Y_k is the mass fraction of the kth species. In addition, p is the pressure, τ_{ij} is the viscous stress tensor, q_i is the heat flux vector, and $V_{k,i}$, and $\dot{\omega}_k$ are the diffusion velocity component and reaction rate of the kth species, respectively. Also, N_s is the total number of chemical species. The governing equations are supplemented by the thermally perfect gas equation of state through $p = \rho RT$, where R is the mixture gas constant and T is the temperature. The specific total energy E in Eq. (2.3) is the sum of the specific kinetic energy and the internal energy, which in turn can be used to relate E and T.

The viscous stress tensor, τ_{ij}, and the heat-flux vector, q_i are given by

$$\tau_{ij} = 2\mu(T)\Big(S_{ij} - \frac{1}{3}S_{kk}\delta_{ij}\Big), \qquad q_i = -\lambda(T)\frac{\partial T}{\partial x_i} + \rho\sum_{k=1}^{N_s} h_k Y_k V_{i,k}, \tag{2.5}$$

where μ is the viscosity, $S_{ij} = \frac{1}{2}\Big(\frac{\partial u_i}{\partial x_j} + \frac{\partial u_j}{\partial x_i}\Big)$ is the strain-rate tensor, λ is the thermal conductivity, and h_k is specific enthalpy of the kth species. The diffusion velocity $V_{k,i}$ for the kth species is given by

$$V_{k,i} = -D_k\frac{1}{X_k}\frac{\partial X_k}{\partial x_i} + \frac{1}{W}\sum_{k=1}^{N_s} D_k W_k \frac{\partial X_k}{\partial x_i}, \tag{2.6}$$

where, W is the mixture molecular weight, and D_k and X_k are diffusion coefficient and mole fraction of the kth species, respectively. The transport properties and the diffusion coefficient for species are obtained through the well-known mixture-averaged formulation (Poinsot and Veynante 2005). The above system of conservation equations is complete after the specification of the initial and boundary conditions.

2.2 Numerical Methodology

The governing equations described in Sect. 2.1 are solved using a well-established three-dimensional (3D) parallel, multi-species compressible reacting flow solver, referred to as AVF-LESLIE (Kim and Menon 2000; Sankaran and Menon 2005). It is a multi-physics simulation tool capable of performing DNS and LES of reacting/non-reacting flows in canonical and moderately complex flow configurations. It has been extensively used in the past to study a wide variety of flow conditions, including acoustic flame-vortex interaction, premixed flame turbulence interaction, non-premixed combustion, and compressible turbulence (Kim and Menon 2000; Sankaran and Menon 2005; Yang et al. 2017a, b; Bowers et al. 2021b; Lowery et al. 2020).

The solver utilizes a finite volume-based spatial discretization of the governing equations in their conservative form on a structured grid using the generalized curvilinear coordinates. The spatial discretization is based on the well-known second-order accurate MacCormack scheme (MacCormack 2003). The time integration of the semi-discrete system of equations is performed by an explicit second-order accurate scheme. The solver can handle arbitrarily complex finite-rate chemical kinetics. The mixture-averaged transport properties, the finite-rate kinetics source terms, and the thermally perfect gas-based thermodynamic properties are obtained using the Cantera software (Goodwin et al. 2014). The parallelization of the solver utilizes the standard domain decomposition technique based on the message-passing interface library. The second-order-accurate spatial discretization has also been used in past studies to examine fundamental aspects of turbulent premixed and non-premixed flames (Yang et al. 2017a, b). This is further illustrated in Appendix A in terms of comparison of results obtained using second- and fourth-order accurate schemes.

3 Description of Computational Setup

We consider a freely propagating methane/air turbulent premixed flame configuration in this study following past studies (Sankaran and Menon 2005; Savre et al. 2013; Ranjan et al. 2016; Yang et al. 2017a; Nilsson et al. 2018; Panchal et al. 2019). Figure 1a shows a schematic of the computational domain. It corresponds to the interaction of an initially one-dimensional (1D) planar laminar methane/air premixed flame with a decaying background isotropic turbulence. The computational domain comprises a 3D cube with the length of the side denoted by L. The initial planar flame is specified to be near the center of the computational domain with the reactants on the left side and the products on the right side of the domain. The initial isotropic turbulence is obtained by evolving the flow field specified using the Kraichnan spectrum (Kraichnan 1970) and re-scaling the evolved velocity field to match the desired turbulence intensity (u'). The value of L is chosen so that $L/l \geq 10$ in all cases, where l is the initial value of the integral length scale of the initial isotropic turbulent flow. The initial flow field is superimposed with the 1D flame solution obtained at $\phi = 0.8$, $T_{\text{ref}} = 570$ K and $p = P_{\text{ref}}$. Here, ϕ, T_{ref}, P_{ref} denote the equivalence ratio, temperature on the unburnt reactants side, and reference pressure, respectively. The effects of an increase in pressure are examined by considering two different values of P_{ref}, namely, 1 atm and 10 atm. The flame conditions, particularly the preheated conditions and the equivalence ratio, chosen here are nominally based on past studies and are typical of gas turbines, spark-ignition engines, and combustors (Sankaran and Menon 2005; Sankaran et al. 2007; Wang and Abraham 2018). A characteristic-based inflow-outflow boundary condition is used in the streamwise (x) direction and a periodic boundary condition is used in the homogeneous

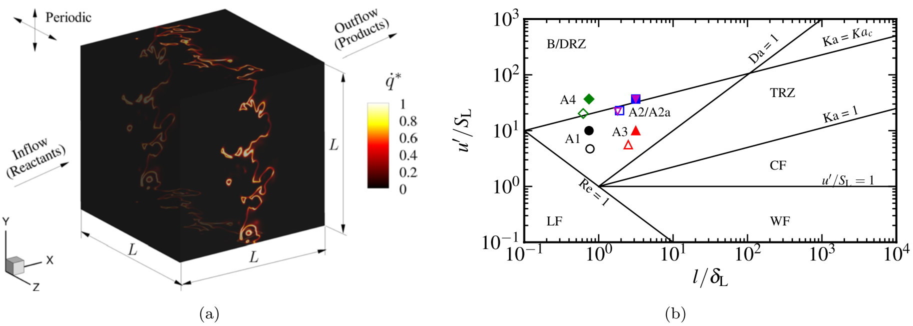

Fig. 1 A schematic of the turbulent premixed flame configuration (**a**) and the premixed regime diagram (Peters 2000) (**b**) for the cases investigated in this study. Here, LF, CF, WF, TRZ, and B/DRZ correspond to laminar flame, corrugated flamelet, wrinkled flamelet, thin reaction zone, and broken/distributed reaction zone regimes, respectively. The schematic in subfigure (**a**) shows the contours of the normalized heat release rate from Case A2, where the normalization is performed using the peak value of the heat release rate of the corresponding laminar flame. In subfigure (**b**), symbols (○), (□), (∇), (Δ), and (◇) denotes cases A1, A2, A2a, A3, and A4, respectively. The solid symbols denote the location on the regime diagram based on the initial state of the turbulence and open symbols denote the state of the isotropic turbulence at $t/t_0 = 2$ when the statistics of flame-turbulence interactions are analyzed. Here, t_0 denotes the initial eddy turnover time

transverse (y) and spanwise (z) directions. At the inflow boundary, no inflow turbulence is prescribed. Therefore, the flame-turbulence interaction is primarily due to the interaction of the flame with the initial isotropic turbulence, which decays with time. A moderately complex four-step and eight-species methane-air mechanism (Smith and Menon 1997) is used in this study to include the effects of finite-rate chemical kinetics. Note that the setup considered here differs from the studies (Hamlington et al. 2011; Savard et al. 2015; Lapointe et al. 2015; Wang and Abraham 2018) where the statistically stationary state of flame-turbulence interactions is achieved through artificial forcing of turbulence.

Table 1 summarizes the key laminar flame, thermodynamic, and transport properties at the two different values of pressure. We can observe that while S_L, δ_L and the kinematic viscosity ν decreases with an increase in pressure, the adiabatic flame temperature (T_{ad}) tends to marginally increase. As expected, it is apparent that ν increases on the products side due to an increase in the temperature. In particular, we can observe that $S_L \sim p^{-0.5}$, $\delta_L \sim p^{-0.5}$, $\rho \sim p$ and $\nu_u \sim p^{-1}$. Note that the changes in the thermodynamic and transport properties with an increase in pressure also affect the background turbulence and therefore, the associated multi-scale flame-turbulence interactions.

We perform DNS of five turbulent premixed flames in this study. These cases are shown on the premixed regime diagram (Peters 2000) in Fig. 1b, and are labeled as A1, A2, A3, A4, and A2a, respectively. As discussed in Sect. 1 these cases are characterized on the regime diagram in terms of the characteristic velocity-scale ratio (u'/S_L) and the characteristic length-scale ratio (l/δ_L). In the regime diagram, the state of flame-turbulence interaction in these cases is shown at the initial time and the time at which statistics are analyzed. For a consistent comparison of the five cases, the statistics are analyzed at $t/t_0 = 2$, where, $t_0 = l/u'$ is the initial eddy turnover time. The cases can also be characterized in terms of the non-dimensional parameters, such as the integral Reynolds number (Re), the Karlovitz number (Ka), and the Damköhler number (Da). Here, the laminar thermal flame thickness is defined as $\delta_L = \frac{(T_b - T_u)}{|\nabla T|_{max}}$, where the subscripts 'b' and 'u' denote burnt and unburnt regions, respectively. Note that the values of all these non-dimensional parameters are based on the conditions of the initial isotropic turbulence.

The simulation parameters for the five cases are summarized in Table 2. Cases A1 and A2a correspond to atmospheric pressure flames and cases A2, A3, and A4 correspond to flames at high pressure. Based on the initial conditions, cases A1 and A3 correspond to the TRZ regime, Case A2 corresponds to the boundary of the TRZ and B/DRZ regime, and Case A4 corresponds to the B/DRZ regime. Note that cases A2 and A2a coincide on the regime diagram and differ in terms of pressure and Re. The difference in Re is due to an increase in u', l, and ν in Case A2a compared to Case A2 to allow for the same values of u'/S_L and l/δ_L in these cases. The five cases are considered to examine the effects of

Table 1 Laminar flame, thermodynamic and transport properties at two different pressures

Parameter	$P_{ref} = 1$ [atm]	$P_{ref} = 10$ [atm]
S_L [m/s]	1.23	0.33
δ_L [mm]	0.33	0.08
T_{ad} [K]	2200	2214
ρ_u/ρ_b [-]	3.76	3.89
$\nu_u \times 10^5$ [m^2/s]	4.8	0.48
$\nu_b \times 10^5$ [m^2/s]	43.5	4.6

Table 2 Simulation parameters for all the cases considered in this study

Case	P_{ref} [atm]	L [mm]	$N_x \times N_y \times N_z$	u'/S_{L}	l/δ_{L}	Re	Ka	Da
A1	1	3.2	$256 \times 256 \times 256$	10.0	0.74	61.3	36.5	0.07
A2	10	3.2	$512 \times 512 \times 512$	36.8	3.15	620.1	126	0.09
A3	10	3.2	$464 \times 464 \times 464$	10.0	3.15	166.3	17.9	0.3
A4	10	0.76	$256 \times 256 \times 256$	36.8	0.74	146.1	259.6	0.02
A2a	10	15	$512 \times 512 \times 512$	36.8	3.15	967	125.8	0.09

an increase in pressure from 1 atm to 10 atm and the changes in the ratio of characteristic scales (u'/S_{L} and l/δ_{L}) at 10 atm. Since an increase in pressure leads to a decrease in S_{L} and δ_{L}, Case A2 is simulated at 10 atm to isolate the effects of pressure while maintaining the same values of l and u' as in Case A1. To analyze the effects of changes in u'/S_{L}, Case A3 is simulated at 10 atm with the same value of l/δ_{L} as in Case A2. To examine the effects of changes in l/δ_{L}, Case A4 is simulated at 10 atm while keeping the value of u'/S_{L} to be the same as Case A2. To examine the effects of change in pressure, while maintaining the same values of u'/S_{L} and l/δ_{L} or Ka, Case A2a is simulated.

The computational domain is spatially discretized using a uniform-size grid, with the number of grid points denoted by N_{x}, N_y, and N_{z} along x–, y–, and z–directions, respectively. The grid resolution is chosen to ensure $k_{\max}\eta \geq 1.5$ and δ_{L} is resolved using at least 10 grid points. Here, $k_{\max}$ and η denote the largest wave number and Kolmogorov length scale of the initial isotropic turbulence. In particular, $k_{\max}\eta$ is 3.5, 2.4, 3.4, 2.2, and 1.5 for cases A1, A2, A3, A4, and A2a, respectively. Also, δ_{L} is resolved using 26, 12, 10, 26, and 11 points in all cases considered in this study. The simulations are carried out up to $t/t_0 = 2$ to allow for spatio-temporal evolution of flame-turbulence interactions. Note that turbulence decays with time in all cases considered here, however, flame-turbulence interactions attain a nearly quasi-stationary state within one or two eddy-turnover times (Savre et al. 2013; Ranjan et al. 2016; Yang et al. 2017a; Nilsson et al. 2018; Panchal et al. 2019), and therefore, such interactions can be examined during such stage. This is discussed further in Appendix B in terms of a comparison of statistics of the temperature field at $t/t_0 = 2$ and 3, where it is observed that the sensitivity of the temperature statistics to the changes in pressure, and length- and velocity-scale ratios remain nearly the same at the two instants.

4 Results and Discussion

In this section, the results from all the cases are discussed at the non-dimensional time, $t/t_0 = 2$. First, the structural features of the reacting flow field are discussed. Afterward, the spatially averaged and state-space representations of the flame structure are described. This is followed by a description of the statistical aspects of the flame-turbulence interactions. Finally, the relationships of the heat release rate with the curvature and the tangential strain rate on the flame surface are analyzed. The results are analyzed to examine the effects of turbulence on the initially planar laminar premixed flame, the increase in pressure when the background turbulence characteristics (l and u') are the same, the changes to

l/δ_L and u'/S_L with the same values of u'/S_L and l/δ_L, respectively, at high pressure, and the effect of increase in pressure for the cases with same value of Ka.

4.1 Structural Features of Flame-Turbulence Interactions

Figure 2 shows the structure of the 3D flame brush for cases A1 and A2. Here, the flame brush is identified using the fuel mass fraction-based progress variable (c), which is defined as:

$$c = \frac{Y_{CH_4} - Y_{CH_4,u}}{Y_{CH_4,b} - Y_{CH_4,u}}. \tag{4.1}$$

Here, $c \in [0,\ 1]$ with $c = 0$ and $c = 1$ corresponding to the reactants and products side, respectively. The flame brush is defined as the spatial extent for $c \in [0.01,\ 0.99]$. Qualitatively, the flame brush from other cases shows similar features, therefore, they are not shown here for brevity. We can observe that in both cases the energetic turbulent eddies lead to an intense wrinkling and stretching of the initially planar flame surface. Although the width of the flame brush increases in the streamwise direction, it varies along

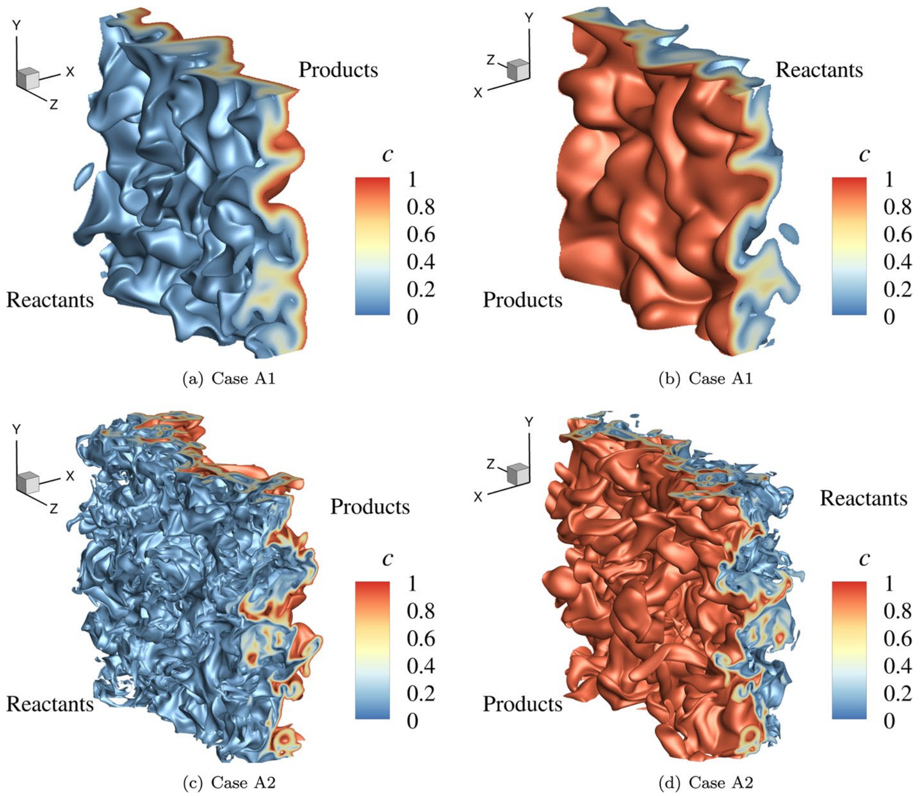

Fig. 2 Structure of the flame brush for cases A1 and A2, identified in terms of the spatial extent for $c \in [0.01,\ 0.99]$. Subfigures **a**, **c** and **b**, **d** correspond to the views from the reactants and the products sides, respectively

the homogeneous y- and z-directions due to the straining effect of the large-scale eddies. This also manifests in the presence of multiple flame crossing along the streamwise (x) direction, particularly in Case A2, which is a characteristic feature of high Ka turbulent premixed flames (Srinivasan and Menon 2014; Ranjan et al. 2016; Ranjan and Menon 2017). The effect of flame-generated thermal expansion is evident from an increase in the overall length scales associated with the reacting flow field across the flame brush, which is due to an increase in the local viscosity on the products side.

The effects of an increase in pressure from Case A1 to Case A2 are apparent in Fig. 2. Although the initial values of l and u' in these cases are the same, the higher pressure in Case A2 results in a higher value of Re and Ka, which implies a decrease in the Kolmogorov length scale. This manifests in an enhanced small-scale wrinkling of the flame and an increase in number of small-scale structures, which has also been reported in past studies of high-pressure turbulent premixed flames (Yenerdag et al. 2015; Wang et al. 2015, 2018; Yilmaz and Gokalp 2017; Savard et al. 2017; Nie et al. 2021). The increase in the range of energetic small scales in high-pressure cases will be described later in terms of the spectral characteristics of the reacting flow field. Quantitatively, the wrinkling, Ξ, of a representative flame surface and the mean flame brush thickness δ_{m} increase in high-pressure cases. Here, $\Xi(t) = A(t)/A(t=0)|_{c=0.8}$, where $A(t)$ denotes the area of the representative flame surface (identified using an iso-surface with $c = 0.8$). Additionally, δ_{m} is defined as the streamwise extent for $\bar{c} \in [0.01,\ 0.99]$, where $\overline{(\cdot)}$ denotes spatial averaging along the homogeneous y- and z-directions (discussed later in Sect. 4.2). In particular, the value of Ξ ($\delta_{\mathrm{m}}/\delta_{\mathrm{L}}$) is 1.6 (3.6), 5 (19.9), 3.6 (16.7), 2.1 (4.6), and 6 (18.5) in cases A1, A2, A3, A4, A2a, respectively. Note that at higher pressure, both S_{L} and δ_{L} decrease, which extends the vortex-flame interaction time and enlarges the extent of the flame turbulence interaction, thus leading to the enhanced wrinkling and flame broadening. As cases A2 and A2a have the same Ka, case A2a shows the effects of high Ka in terms of increased values of Ξ and $\delta_{\mathrm{m}}/\delta_{\mathrm{L}}$. However, we observe quantitative differences in these cases due to a difference in pressure and Re. Although Ξ tends to be higher in Case A2a compared to Case A2, the enhanced small-scale transport at high pressure leads to a higher value of $\delta_{\mathrm{m}}/\delta_{\mathrm{L}}$. This difference can be attributed to the flame-surface wrinkling being dominated by large scales of motion. In Case A3, the values of Ξ and $\delta_{\mathrm{m}}/\delta_{\mathrm{L}}$ are reduced compared to Case A2, because of a decrease in the value of u'/S_{L}, which decreases the ability of the eddies to wrinkle the flame surface and to transport heat and mass away from the heat release region. These quantities are reduced further in Case A4, even though Ka is the highest in this case. Note that in this case the value of l is decreased compared to Case A2, which affects the amount of large-scale wrinkling and stretching of the flame surface.

The effects of pressure and the characteristic scale ratios on the structure of the flame are also evident from the contours of the normalized temperature ($T^* = T/T_{\mathrm{ad}}$) in the central $x-y$ plane, which are shown in Fig. 3. The spatial coordinates are normalized as $x^* = (x - x_0(t))/\delta_{\mathrm{L}}$, and $y^* = y/\delta_{\mathrm{L}}$ with $x_0(t)$ being the mean global flame position (Aspden et al. 2011) defined as

$$x_0(t) = \frac{1}{L^2\left(\rho Y_{\mathrm{CH_4}}\right)_{\mathrm{u}}} \int_{\mathcal{V}} \rho Y_{\mathrm{CH_4}} d\mathcal{V}, \tag{4.2}$$

where $\mathcal{V}$ denotes the computational domain. The contours of the temperature field are overlaid with the flame brush extents to represent the flame structure on this plane.

In the high-pressure cases, particularly cases A2 and A3, we can observe a much sharper variation of the temperature compared to cases A1 and A2a, which leads to these

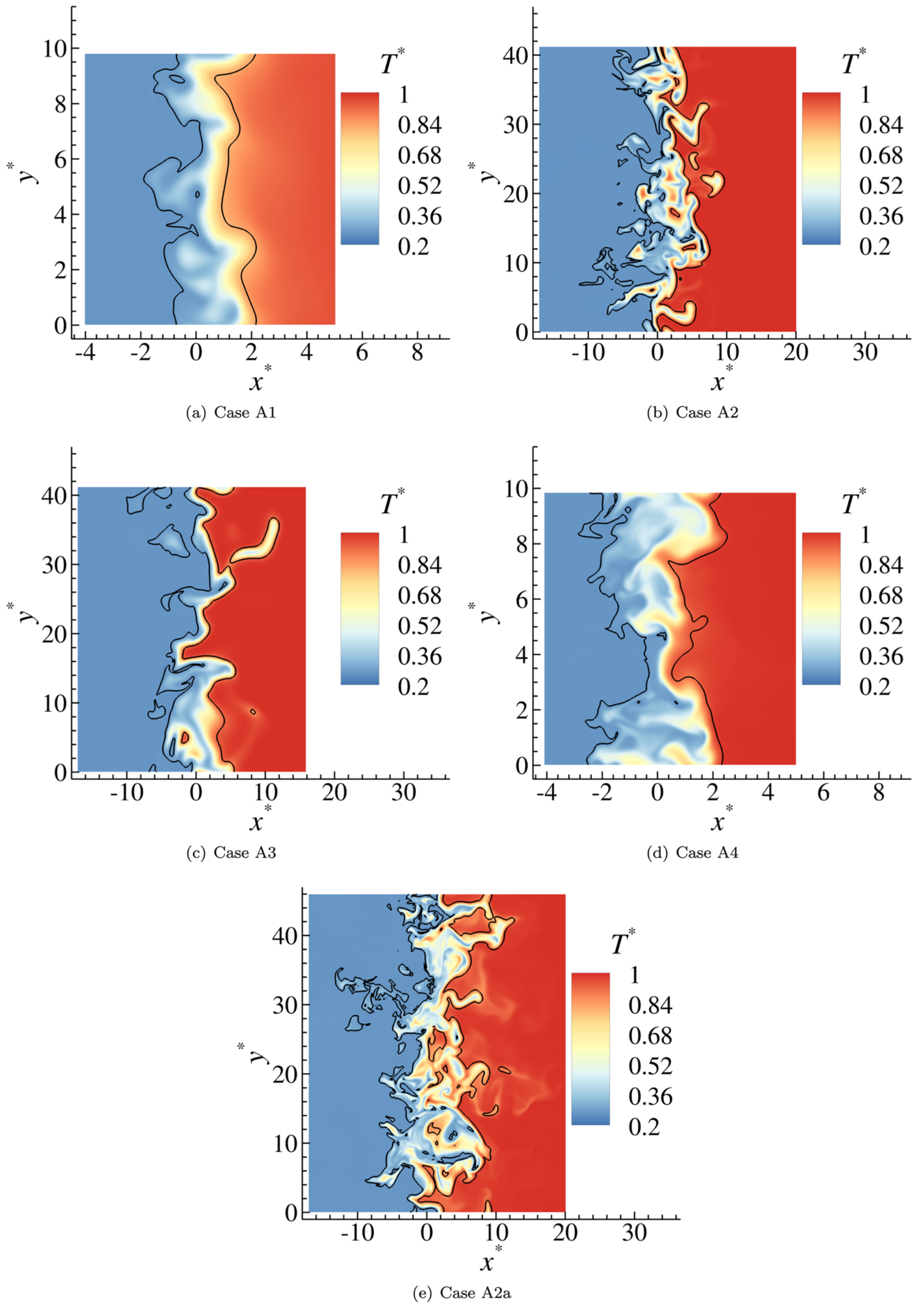

Fig. 3 Contours of the normalized temperature T^*, in the central $x - y$ plane overlaid with the flame brush, which is identified as the region within $c \in [0.01,\ 0.99]$

cases attaining the post-flame temperature within a shorter streamwise extent. Similar to Fig. 2, an enhanced small-scale wrinkling and broadening of the flame due to an increase in pressure is evident in cases A2 and A3. Furthermore, in Case A2, we can notice a less defined flame front with pockets of high temperature in the preheat zone, multiple flame crossings in terms of variation of temperature, and an increased normalized streamwise extent of mean flame brush, i.e., $\delta_{\mathrm{m}}/\delta_{\mathrm{L}}$ by about 5.5 times compared to Case A1, which results from the enhanced transport of heat and mass, particularly in the preheat region. Although such a behavior has been reported in the past studies for high *Ka* turbulent premixed flames at atmospheric pressure (Aspden et al. 2011; Srinivasan and Menon 2014; Savard et al. 2015; Lapointe et al. 2015; Wabel et al. 2017; Wang et al. 2017), here, the enhanced small-scale wrinkling due to high-pressure further contributes to the modifications of the flame structure. Note that while cases A2 and A2a show some similarity in the qualitative behavior of the contours of the temperature field, there are differences as well. For example, the temperature increase is gradual in Case A2a compared to Case A2, and $\delta_{\mathrm{m}}/\delta_{\mathrm{L}}$ is about 8% higher in Case A2 compared to Case A2a, thus implying a dominant role of the energetic smaller scales of motion in Case A2 on the enhancement of transport of heat and mass. This will be discussed later in terms of the spectral distribution of turbulent kinetic energy.

Qualitatively, similar behavior of the temperature field and the flame brush is observed in cases A2 and A3. However, the variation of the temperature field is smoother and the flame front is less disrupted in Case A3 due to a lower value of u'/S_{L}, which reduces the amount of wrinkling (Klein et al. 2018). Although the value of *Ka* is highest in Case A4, the contours of the temperature field and the variation of the flame brush show qualitatively similar behavior as Case A1. These results demonstrate that the characteristic scales play a significant role in affecting the spatial variation of the flame structure. In Case A4, l/δ_{L} is decreased compared to Case A2 while maintaining the same value of u'/S_{L}. Therefore, a well-defined flame front with a small amount of wrinkling is observed due to a decrease in the overall range of scales of motion. Such a behavior has been observed in a past study (Klein et al. 2018), where at elevated pressures, decreasing l/δ_{L} resulted in a more stable flame structure. Qualitatively, the spatial distribution of flame brush and the variation of temperature field in all cases as shown in Fig. 3 indicates a strong correlation of c and T, which will be discussed further in Sect. 4.3.

The presence of the flame affects the background turbulence, which is shown in Fig. 4 in terms of the contours of the normalized vorticity magnitude, $\omega^* = |\boldsymbol{\omega}|l/u'$. As expected, due to an increase in the local viscosity on the products side due to heat release, the small-scale structures get dissipated in all cases. Note that an increase in pressure at a fixed temperature leads to a decrease in the Kolmogorov length scale or an increase in the local Reynolds number. This results in the appearance of small scales in the vorticity field in the preheat region of cases A2 and A3. The small-scale structures in the preheat region of Case A1 get dissipated within the flame brush region, however, in the high-pressure cases, particularly, in Case A2, the energetic small-scale eddies are also observed in the post-flame region. Similar to the variation of the temperature field shown in Fig. 3, in Case A4, the contours of the vorticity field tend to show features very similar to Case A1, where the small-scale eddies get dissipated across the flame brush. Qualitatively, the variation of ω^* tends to be similar in cases A2 and A2a which have same values of *Ka*, however, ω^* tends to have higher values in Case A2a, which can be attributed to a higher initial value of *Re* in this case.

To examine the contribution of various length scales to the kinetic energy and to understand the role of pressure on such contributions, we examine the specific spectral

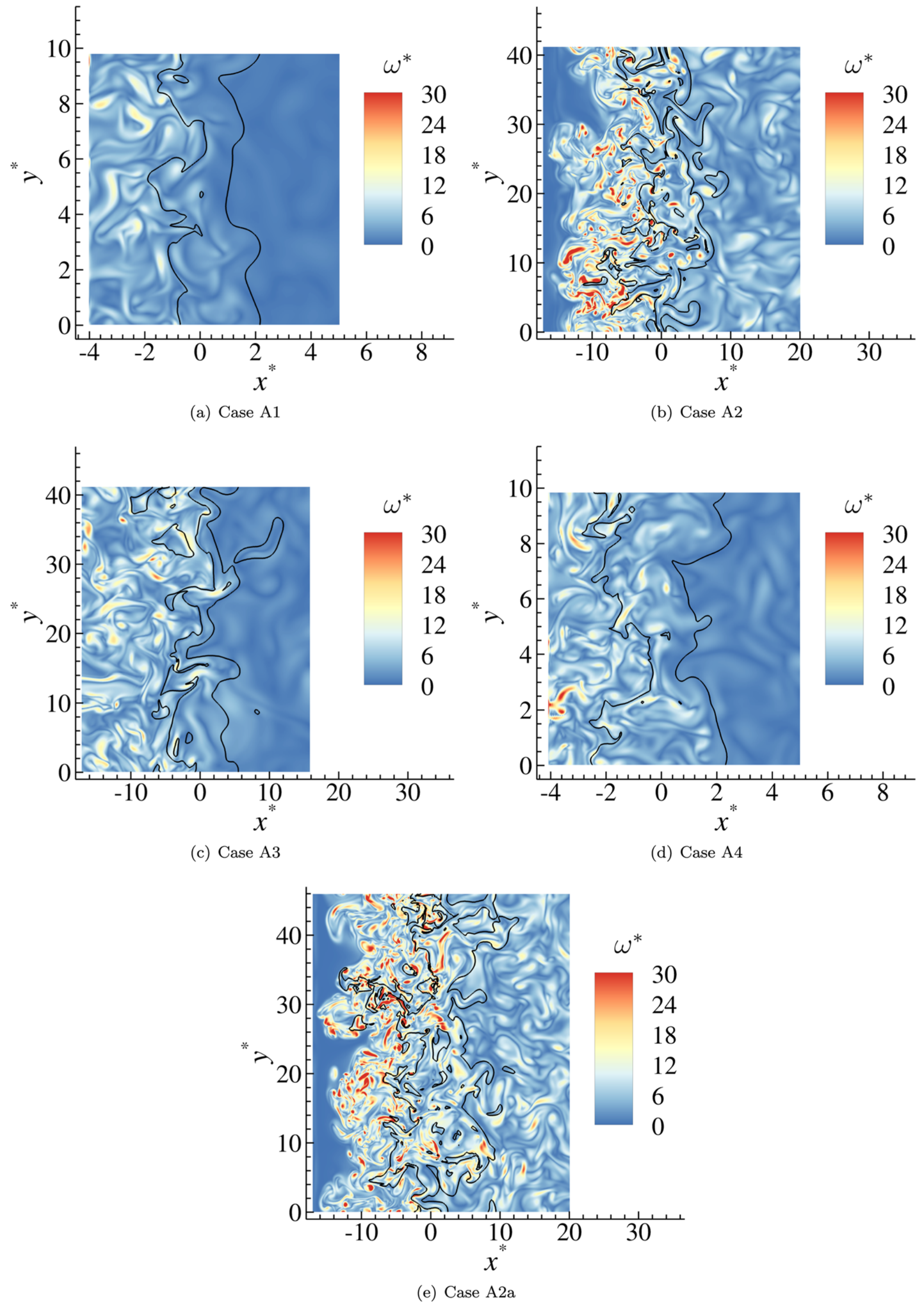

Fig. 4 Contours of the normalized magnitude of vorticity ($\omega^* = |\boldsymbol{\omega}|l/u'$) in the central $x-y$ plane overlaid with the flame brush

kinetic energy (SKE) across the flame brush. Following the past study by Towery et al. (2016), SKE is defined as: $\widehat{E}(\boldsymbol{\kappa}_{\mathrm{p}}, t, \bar{c}) = \left\langle \frac{1}{2}\widehat{u}_i^* \widehat{u}_i \middle| \bar{c} \right\rangle$. Here, $\widehat{(\cdot)}$ denotes two-dimensional (2D)

Fourier transform, $\boldsymbol{\kappa}_\mathrm{p}$ is the wave vector with the magnitude denoted by κ_p, and $\langle \cdot | \overline{c} \rangle$ denotes conditional average on $\overline{c}(x,t)$, where $\overline{c}$ is the spatially averaged (along homogeneous y and z directions) progress variable. Note that there is a direct correspondence between x and $\overline{c}$ in the present cases, and therefore, $\overline{c}$ alone is used to indicate the location in the flame brush.

Figure 5 shows the SKE distribution at three locations within the flame brush region. In all cases, we observe substantial changes to the SKE distribution across the flame brush. In particular, the SKE associated with the small scales of motion is suppressed and that associated with the large scales of motion is enhanced on the products side. We observe that for $2 \lessapprox \kappa_p l \lessapprox 5$, SKE reduces gradually on the reactants side whereas it stays nearly constant on the products side. Similarly, we observe that for $\kappa_p \gtrapprox 20$, the value of SKE tends to be lower on the products side. The suppression of SKE of the small scales is due to heat release, which leads to thermal expansion and a corresponding increase in viscosity. On the reactants side, we observe a small region with $-5/3$rd inertial range scaling, but such scaling is not evident at the other two locations. The increase in pressure in Case A2 compared to Case A1 leads to a broader range of scales of motion with the smaller scales being more energetic. This is evident at all three locations and similar behavior has also been observed in past studies of turbulent premixed flames at high pressure (Fragner et al. 2015; Yilmaz and Gokalp 2017). The decrease in u'/S_L in Case A3 compared to Case A2 yields expected behavior with lower energy of the small scales. The extent of small scales of motion in Case A4 is reduced due to a corresponding decrease in the integral length scale. Such a decrease in the range of scales of motion in Case A4 affects the wrinkling of the flame surface as discussed before. The effect of pressure differences in cases A2 and A2a is also evident from the SKE distribution at all three locations. In particular, the SKE is higher in Case A2a for all scales of motion except the smaller scales. The range of energetic smaller scales of motion is larger in Case A2 compared to Case A2a, which in turn affects the small-scale mixing and transport of heat from the flame region. This affects the flame brush broadening as discussed before, which is about 8% more in Case A2 compared to Case A2a.

The results of the flame and flow structures discussed in this section highlight the highly nonlinear and multi-scale nature of flame-turbulence interactions and the effects of pressure and characteristic scales on such interactions. Although the features of such interactions at high pressure while maintaining the same background turbulence tend to show similarity with high *Ka* flames at atmospheric pressure, the higher value of pressure increases the complexity of the interactions due to an increase in the small-scale wrinkling and transport associated with the energetic small-scales of motion. This is also apparent

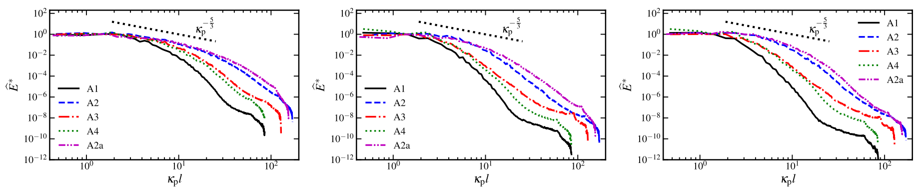

(a) Reactants ($\overline{c} = 0.1$) (b) Flame front($\overline{c} = c_\mathrm{m}$) (c) Products ($\overline{c} = 0.97$)

Fig. 5 Normalized spectral kinetic energy ($\widehat{E}^* = \widehat{E}(\kappa_\mathrm{p}, c_\mathrm{f})/\widehat{E}_0$) on the reactants (**a**), the flame front (**b**), and the products (**c**) sides. Here, $\widehat{E}_0 = \widehat{E}(\kappa_\mathrm{p} = l^{-1})$ is used for normalization. The spectra are obtained at specific values of $\overline{c}$ within the flame brush region. Here, c_m denotes the value of c corresponding to the peak location of the conditionally averaged heat release rate. A reference dotted line with $\kappa_\mathrm{p}^{-5/3}$ spectral slope is also included from the observed differences in cases A2 and A2a, which have the same *Ka* but differ in the operating pressure. A quantitative description of such interactions is discussed in the next sections.

4.2 Spatially Averaged Flame Structure

Now, we analyze the spatially averaged flame structure, where the spatially averaged quantities are obtained by averaging along the homogeneous *y*- and *z*-directions through

$$\overline{\psi}(x,t) = \frac{1}{L^2}\int_0^L\int_0^L \psi(x,y,z,t)\,dy\,dz. \tag{4.3}$$

Here, ψ denotes thermo-chemical quantities such as progress variable, temperature, mass fraction of species, etc. Figure 6 shows the streamwise profile of several thermo-chemical quantities, where the results from the corresponding laminar premixed flames are also included to demonstrate the effects of turbulence.

A noticeable spatial broadening of the flame brush compared to the corresponding laminar flames is apparent from the streamwise variation of all the quantities, which is consistent with the 3D and 2D flame structures discussed before in Sect. 4.1. It is a well-known feature of the turbulent premixed flames in the TRZ and B/DRZ regimes (Aspden et al. 2011; Srinivasan and Menon 2014; Savard et al. 2015; Lapointe et al. 2015; Wabel et al. 2017; Ranjan et al. 2016; Wang et al. 2017). The broadening of the mean flame brush leads to the presence of mixed partially burned and unburnt fluid ahead of the mean global flame position. Note that the spatial broadening observed here is associated with the broadening of the profile of $\overline{c}$ and it differs from the local flame thinning in high-pressure cases, which is discussed later in Sect. 4.3.

The variation of $\overline{c}$ and $\overline{T}$ along the *x*-direction is sensitive to the pressure and the characteristic scales. In the high-pressure cases, particularly, cases A2 and A3, higher values of $\overline{c}$ and $\overline{T}$ are observed ahead of the mean flame location ($x^* \approx 0$) compared to the atmospheric pressure flames (cases A1 and A2a). This is due to the presence of energetic eddies that are smaller in size in these cases, which lead to enhanced transport of heat and mass away from the heat release region to the preheat region. The effect of pressure for the same values of u'/S_L and l/δ (cases A2 and A2a) is apparent mainly in the post-flame region, where the temperature variation is more gradual in Case A2a with an overall higher temperature than that observed in Case A2. The effects of change in u'/S_L and l/δ_L are more pronounced beyond $x^* \approx 0$, although some sensitivity is also noticeable in the preheat region. For example, compared to Case A2, in Case A3 the effect of homogenization by small-scale eddies is reduced due to a decrease in u'/S_L, which is similar to the well-known behavior observed in atmospheric pressure flames (Savre et al. 2013; Ranjan et al. 2016). On the other hand, the decrease of l/δ_L in Case A4 reduces the large-scale modification of the flame surface causing the overall mean flame brush extent to decrease compared to cases A2 and A3. Similar to the 2D and 3D flame structures discussed in Sect. 4.1, the variation of $\overline{c}$ and $\overline{T}$ in Case A4 is closer to Case A1, although a sharper variation of $\overline{T}$ is observed in Case A4 in the post-flame region. A high degree of correlation between $\overline{c}$ and $\overline{T}$ is evident from the profiles of these quantities in all cases, which will be discussed further in Sect. 4.3 in terms of the state-space variation.

The variation of other quantities, which include the heat release rate ($\dot{q}$), mass fraction of major (CO_2), and intermediate (CO and H_2) species also show the effects of pressure

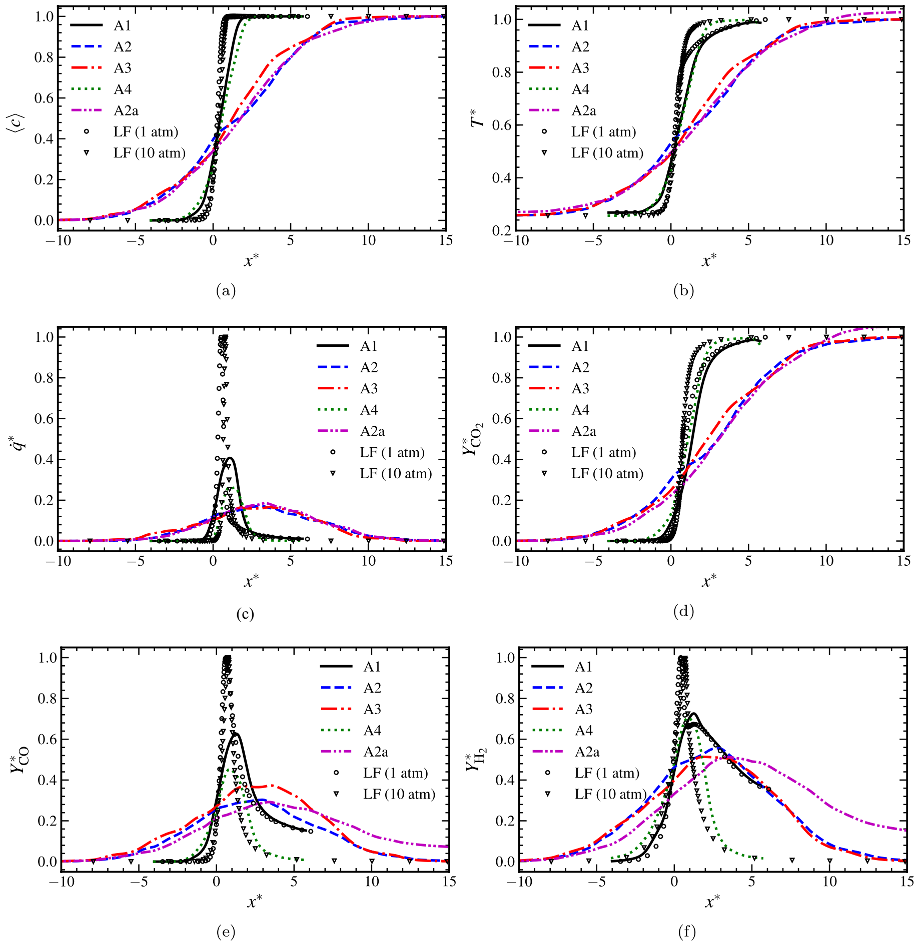

Fig. 6 Spatially averaged profile of progress variable (**a**), temperature (**b**), heat release rate (**c**), and mass fraction of CO_2 (**d**), CO (**e**), and H_2 (**f**). Results from laminar flames at 1 atm and 10 atm are also included. The superscript * indicates the normalization of a quantity by the corresponding peak laminar value of the quantity

and the changes to the characteristic scales. The peak value of $\dot{q}$ decreases in all cases compared to the corresponding laminar flames, which is a well-known feature of turbulent premixed flames. The increase in pressure with the same background turbulence leads to a broader flame structure. The effects of changes in the characteristic scale ratios at high pressure are much more apparent when l/δ_{L} is reduced in Case A4 causing an increase in the peak value of $\dot{q}$ compared to cases A2 and A3. The streamwise variation of the mass fraction of CO_2 shows a similar behavior as observed for $\overline{T}$ in Fig. 6b. Although the spatial variation of $\dot{q}$ in cases A2 and A2a is nearly the same, differences are evident in the spatial variation of CO_2 in these cases, particularly in the preheat and post-flame regions. Note that these cases have the same values of u'/S_{L} and l/δ_{L}, but they differ in *Re* and range of scales of motion, which affects the flame-turbulence interactions in a different manner.

As expected, the intermediate species (CO and H_2) exhibit a behavior similar to the variation of $\dot{q}$, where the increase in pressure leads to a reduction in the peak value and a broader profile compared to the corresponding laminar flames. In the high-pressure cases, CO is completely oxidized into CO_2 in the post-flame zone. However, CO emission is observed in the atmospheric pressure flames (cases A1 and A2a), which is due to a gradual increase in the temperature (see Fig. 6b). However, in Case A2a, the amount of CO is significantly reduced compared to Case A1 demonstrating the role of enhanced turbulent transport in this case. Note that CO requires a high temperature to oxidize, which tends to be the case in all high-pressure flames and Case A2a leading to its spatially earlier oxidation. These results demonstrate that the turbulence scales affect the spatial variation of the intermediate species significantly. Additionally, the effect of pressure in cases A2 and A2a, which have the same value of Ka, is much more apparent in the variation of the intermediate species, which again demonstrates the differences in these cases due to the range of scales of motion and the turbulent kinetic energy associated with such scales.

We observe that the increase in pressure and changes in the characteristic scale ratios at high pressure lead to significant modifications to the spatially averaged flame structure. While the presence of turbulence spatially broadens all the flames, the increase in pressure affects the transport further. At high pressure, the changes to the length scale ratio have pronounced effects compared to the changes in the velocity scale ratio. Next, we describe the flame structure in the state space.

4.3 State-Space Representation

The flame-front-based models such as the flamelet-progress variable approach (Bradley et al. 1988; Maas and Pope 1992; Van Oijen and Goey 2000; Peters 2000) rely on the notion that the variation of thermo-chemical quantities such as species mass fraction and temperature can be represented in terms of a reaction progress variable and its variance. Therefore, we analyze the flame structure by considering the variation of several thermo-chemical quantities with respect to the progress variable, which is shown in Fig. 7.

As discussed in Sect. 4.2, we observe a very good correlation between the normalized temperature (T^*) and the progress variable (c) in Fig. 7a across most of the flame brush region in all cases except cases A2 and A2a. The increase in the pressure in the laminar flame is apparent from a relatively lower value of T^* in most of the flame regions except in the vicinity of the heat release and post-flame regions. An abrupt increase in the value of T^* occurs in all cases for $c \gtrapprox 0.95$. In Case A2, higher values of the T^* are observed compared to the other high-pressure cases and the corresponding laminar flame in the vicinity of the reaction zone (identified by the peak location of $\dot{q}$). This can be attributed to the enhanced transport of heat and the small-scale wrinkling compared to the other cases. Note that even though cases A1 and A2 have the same initial value of u' and l, the wide range of small scales in Case A2 leads to the observed variation of T^* with respect to c due to increased Ka. Such a behavior is a well-known feature of high Ka flames, where turbulent mixing dominates over molecular diffusion and the increase in pressure further contributes to this (Day et al. 2009; Aspden et al. 2011; Lapointe et al. 2015; Savard et al. 2015; Ranjan et al. 2016). A similar behavior is also observed in Case A2a, where enhanced transport of heat occurs due to a higher Re, which leads to higher values of T^* compared to Case A2 throughout the flame brush region. The other cases follow the quasi-linear variation of T^* with respect to c, with negligible sensitivity to the changes in the characteristic scale ratios at high pressure.

Although the sensitivity to changes in u'/S_{L} and l/δ_{L} tends to be negligible for the variation of T^* with c at high pressure, it is much more apparent in the variation of other

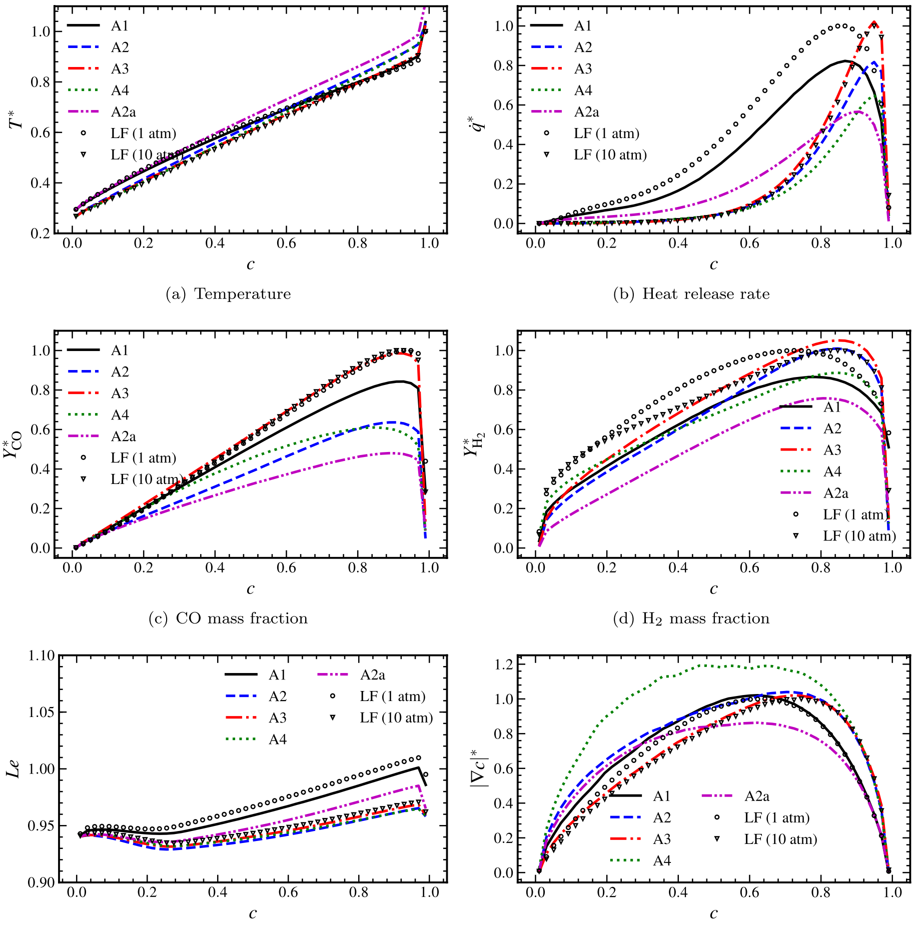

(a) Temperature (b) Heat release rate (c) CO mass fraction (d) H_2 mass fraction (e) Le (f) SDF

Fig. 7 Conditional variation of normalized temperature (**a**), heat release rate (**b**), mass fraction of CO (**c**), mass fraction of H_2 (**d**), Lewis number of CH_4 (**e**), and surface density function (SDF) (**f**) with respect to the progress variable. The normalization of a quantities in subfigures (**a**–**d**) and (**f**) is performed using the peak value of the corresponding laminar flame

quantities, such as the normalized heat release ($\dot{q}^*$) and the intermediate species mass fractions shown in Fig. 7b–d. Similar to the laminar flame, the increase in pressure leads to a compact flame structure in the state space, which is apparent from the variation of $\dot{q}^*$ in all high-pressure cases. The peak value of $\dot{q}^*$ shifts to a higher value of c, or, higher values of T^* (since c and T^* are highly correlated), and the heat release at low c is decreased, which usually occurs in high-pressure and high Ka flames (Carlsson et al. 2014; Dinesh et al. 2016; Wang et al. 2018). The dominant role of turbulent diffusion over molecular diffusion is evident in all cases here, except in Case A3. Note that the effect of differential molecular diffusion is present in all cases, however, it tends to affect the flames at high pressure more. The behavior in Case A3, where values closer to laminar flame are observed, is due to a decrease of u'/S_L. However, contrary to the spatial flame structure discussed in Sect. 4.2, where the spatially averaged flame structure in Case A4 showed similarity to Case A1, we observe significant differences between these cases in the state space, particularly in terms of a compact flame structure and a shift in the peak of $\dot{q}^*$ towards higher c. Although cases A2 and A2a have the same Ka, they tend to differ substantially in terms of the variation of $\dot{q}^*$ with respect to c, which can be attributed to a higher Re in Case A2a, the role of differential diffusion, and the enhanced small-scale wrinkling at high pressure.

The variation of mass fraction of CO clearly shows the effects of pressure and changes of the characteristic scale ratios in all cases except Case A3, which follows the corresponding laminar variation. However, even in this case, the variation of H_2 deviates from the laminar variation, particularly in the preheat region, thus indicating the dominance of turbulent diffusion over differential diffusion. The competing effects of turbulent diffusion and molecular diffusion lead to significant changes in the variation of the mass fraction of H_2. While at atmospheric pressure the normalized mass fraction of H_2 is lower than the corresponding laminar flame across the flame, it is comparable to or higher than the laminar values in the vicinity of the heat release region in cases A2 and A3. Similar to Case A1, Case A4 shows lower values of mass fraction of H_2 throughout the flame implying the effects of turbulence scales at high pressure. The cases A2 and A2a, which have the same *Ka,* show significant differences in the variation of CO and H_2. An increase in pressure leads to higher values of these species throughout most of the flame region.

The role of differential diffusion on the flame structure can be understood in terms of the Lewis number (Le), which we define here as the ratio of thermal diffusivity ($\lambda/\rho C_\mathrm{p}$) to the mass diffusivity of the deficient reactant (D) (Clavin and Williams 1982; Abdel-Gayed et al. 1985; Ashurst et al. 1987; Haworth and Poinsot 1992; Rutland and Trouvé 1993). As all cases in the present study corresponds to lean conditions, CH_4 is considered as the deficient reactant to determine Le. Note that $Le < 1$ implies a higher diffusion of the species compared to the thermal diffusion, which under laminar or moderate turbulence conditions can lead to the occurrence of thermo-diffusive instability. In all cases, we observe $Le \lessapprox 1$ throughout the flame brush region, however, Le approaches value closure to unity in the vicinity of the heat release region. The effect of turbulence is apparent in terms of a slightly lower value of Le throughout the flame region compared to the corresponding laminar flames, which leads to enhanced transport of reactants from low temperature region towards the flame causing an enhanced wrinkling of the flame surface. However, the deviation of Le from the corresponding laminar values tends to be small, thus indicating a dominant role of turbulent diffusion over differential diffusion as discussed before. The effect of change in pressure on the variation of Le is more apparent compared to the changes in u'/S_L and l/δ_L at high pressure. In all high-pressure cases, Le is lower compared to atmospheric pressure flames, which indicates an enhanced transport and small-scale wrinkling of the flame surface as discussed before.

The flame-front-based modeling of turbulent premixed flames relying on the closure of the generalized FSD Boger et al. (1998) and the scalar dissipation rate (Chakraborty et al. 2011) depends upon the surface density function (SDF), $|\nabla c|$Kollmann and Chen (1998). The state-space variation of SDF also indicates a local thickening/thinning of the flame. The variation of normalized SDF is shown in Fig. 7e. The effect of an increase in pressure on laminar flame is apparent from an increase in the value of SDF for all values of c indicating a local flame thinning (not shown here). The peak value of SDF increases from 4897.1 m^{-1} to 15928.5 m^{-1} due to an increase in the pressure in the laminar flames. This behavior is also evident in the turbulent premixed flames considered here except in Case A2a, which has also been observed in past studies in terms of an increase in the peak value of FSD (Lachaux et al. 2005; Wang et al. 2015; Yilmaz and Gokalp 2017; Cecere et al. 2018; Ichikawa et al. 2019; Nie et al. 2021). While in Case A1, the variation of SDF with

c is closer to the corresponding laminar flame variation, in Case A2, local flame thinning is evident primarily in the preheat region. Such a local flame thinning in the preheat region is also observed in Case A2a, although significant differences are observed between cases A2 and A2a for $c \gtrapprox 0.3$. The effect of changes in the characteristic scale ratios at high pressure is also evident, where due to a decrease in u'/S_L in Case A3, the variation of SDF follows the laminar flame, but a decrease in l/δ_L in Case A4, leads to enhanced gradients of the progress variable, i.e., local flame thinning. This implies that the straining effect of turbulent eddies is dominant compared to the mixing in this case. Note that thinning or comparable behavior to a laminar flame described here differs from the spatial flame broadening discussed in Sects. 4.1 and 4.2, which is due to the spatial broadening of the progress variable itself.

The state-space representation of the flame structure discussed in this section illustrates the sensitivity to pressure as well as the changes in the characteristic scale ratios at high pressure. The differences in the state-space representation of thermo-chemical quantities in cases A2 and A2a show that even though these cases coincide on the regime diagram, the nonlinear flame-turbulence interactions get affected by the increase in pressure and a difference in Re in these cases. These results demonstrate the need for an accurate representation of these effects while considering a low-dimensional manifold representation or flame-front-based modeling of such flames.

4.4 Flame Statistics

The flame-turbulence interaction is now examined in terms of normalized PDFs of reaction zone thickness ($\delta_{0.5}$), tangential strain rate (a_T), curvature (κ), density gradient magnitude ($|\nabla\rho|$), and heat release rate, which are shown in Fig. 8. The quantities $\delta_{0.5}$, κ and a_T are defined as

$$\delta_{0.5} = \frac{T_\mathrm{b} - T_\mathrm{u}}{\left.\frac{\partial T}{\partial x_i}\right|_{c^*=0.5}}, \qquad \kappa = \left.\frac{\partial n_i}{\partial x_i}\right|_{c=c_\mathrm{max}}, \qquad a_\mathrm{T} = \left.\left[\frac{\partial u_k}{\partial x_k} - n_i n_j \frac{\partial u_i}{\partial x_j}\right]\right|_{c=c_\mathrm{max}}. \tag{4.4}$$

Here, c^* is a temperature-based progress variable defined as: $c^* = (T - T_\mathrm{u})/(T_\mathrm{b} - T_\mathrm{u})$ and c_max corresponds to the value of c at which peak of $\dot{q}$ is observed in Fig. 7. The value of c_max is 0.87, 0.95, 0.95, and 0.95 for cases A1, A2, A3, and A4, respectively. Additionally, n_i is the ith component of the unit normal vector to the flame front towards the reactants given by $\boldsymbol{n} = -\boldsymbol{\nabla} c/|\boldsymbol{\nabla} c|$. Compared to other PDFs, which are extracted at the representative flame surface (either $c^* = 0.5$ or $c = c_\mathrm{max}$), the PDF of $|\boldsymbol{\nabla}\rho|$ is obtained using the entire 3D data. The PDFs are obtained using the non-dimensionalized quantities, which are given by

$$\delta^*_{0.5} = \delta_{0.5}/\delta^\mathrm{L}_{0.5}, \qquad \kappa^* = \kappa\delta_\mathrm{L}, \qquad a^*_T = a_T\tau_\eta, \tag{4.5}$$

where $\delta^\mathrm{L}_{0.5}$ is the laminar reaction zone thickness, and τ_η is the initial Kolmogorov time-scale. The first three moments of these quantities, namely, mean (μ), standard deviation (σ), and skewness (γ) for all cases are summarized in Table 3.

In all cases, the PDF of normalized $\delta^*_{0.5}$ shown in Fig. 8a, exhibit a positively skewed behavior. The normalization is performed by using the standard deviation (σ) of $\delta^*_{0.5}$. The PDFs tend to exhibit a log-normal behavior in all cases and indicate the presence of both localized thickening/thinning of the reaction zone. The log-normal behavior of the PDF of $\delta^*_{0.5}$ is a well-known feature of turbulent premixed flames in the TRZ regime (Yuen and

Table 3 Mean (μ), standard deviation (σ), and skewness (γ) of $\delta^*_{0.5}$, κ^*, a^*_T, $\nabla\rho\delta_L/(\rho_u-\rho_b)$, and $\dot{q}^*$ for all cases

Case	$\delta^*_{0.5}$			κ^*			a^*_T			$\nabla\rho\delta_L/(\rho_u-\rho_b)$			$\dot{q}^*$		
	μ	σ	γ	μ	σ	γ	μ	σ	γ	μ	σ	γ	μ	σ	γ
A1	0.9	0.3	2.5	0.04	2.4	1.5	0.2	0.2	−0.06	0.22	0.5	2.1×10^{-3}	0.84	0.2	−0.4
A2	0.9	0.7	5.4	0.34	2.6	2.3	0.6	0.7	0.31	0.17	0.4	6.4×10^{-5}	0.8	0.3	0
A3	1.0	0.4	5	0.12	1.4	1.8	0.3	0.3	0.25	0.1	0.3	6.1×10^{-5}	0.98	0.1	0.8
A4	0.7	0.5	3.9	0.13	3.7	2.3	0.5	0.5	0.05	0.34	0.7	5.5×10^{-5}	0.64	0.2	0
A2a	1.0	0.8	4.7	0.57	3.3	1.6	0.4	0.6	0.36	0.18	0.5	2.8×10^{-3}	0.55	0.2	0.3

Gülder 2009). Note that the thickening of the reaction zone occurs due to a broad range of the temperature gradient in the reaction zone with a magnitude smaller than the laminar variation due to mixing, and the thinning occurs due to the stretching of the flame front by the turbulent eddies. The stretching of the flame surface creates a sharp interface between reactants and products (Yuen and Gülder 2009; Aspden et al. 2011), which can also be seen in Figs. 2 and 3. The increase in pressure affects the shape of the PDF of $\delta^*_{0.5}$ in terms of an increase in the values of σ and γ compared to Case A1 (see Table 3). The behavior of the PDF in Case A2a tends to be very similar to Case A2, which implies the role of enhanced transport and stretching due to high *Re* in this case. The value of μ shows minor sensitivity to the increase in pressure and is much more sensitive to the change in the value of l/δ_L. For example, in Case A4, the value of μ decreases, which implies that the straining effect of turbulent eddies is dominant compared to the mixing effects in the reaction zone in this case.

The thickening/thinning of a local flame element is a result of competing effects of κ and a_T (Sankaran et al. 2007; Yuen and Gülder 2009; Wang et al. 2017). For example, a positive value of a_T causes thinning, whereas a positive value of κ leads to a thickening of a premixed flame. The PDFs of normalized curvature (κ^*) and tangential strain-rate (a^*_T) are shown in Fig. 8b and c to understand these features of the local flame elements.

The role of κ on the flame propagation and the burning rate has been extensively studied in the past (Trouve and Poinsot 1994; Echekki and Chen 1996; Sankaran and Menon 2005; Sankaran et al. 2007; Yuen and Gülder 2009). The regions of flame having a convex/concave shape towards reactants lead to a focusing/de-focusing effect, which increases/decreases the local reaction rate and the flame propagation speed. In all cases, the mean value of κ is positive (see Table 3) although both positive and negative values of curvature are probable as evident from the presence of both convex and concave flame elements in the instantaneous flame structure shown in Figs. 2 and 3. The increase in pressure in Case A2 leads to an increase in the value of all three moments compared to Case A1. This is associated with an increase in the probability of convex structure with higher values (Wang et al. 2015, 2018; Dinesh et al. 2016; Cecere et al. 2018), which is due to the enhanced small-scale wrinkling (Soika et al. 2003; Lachaux et al. 2005). The PDFs from high-pressure cases also show sensitivity to the change in the values of l/δ_L and u'/S_L. Compared to the past studies of low-pressure flames, where an increase in *Ka* causes the PDF of curvature to approach a Gaussian due to an increasing effect of turbulent mixing (Yuen and Gülder 2009; Aspden et al. 2011; Sankaran et al. 2007), at high-pressure we do not observe such a behavior. Qualitatively, cases A2 and A2a show similar behavior of the

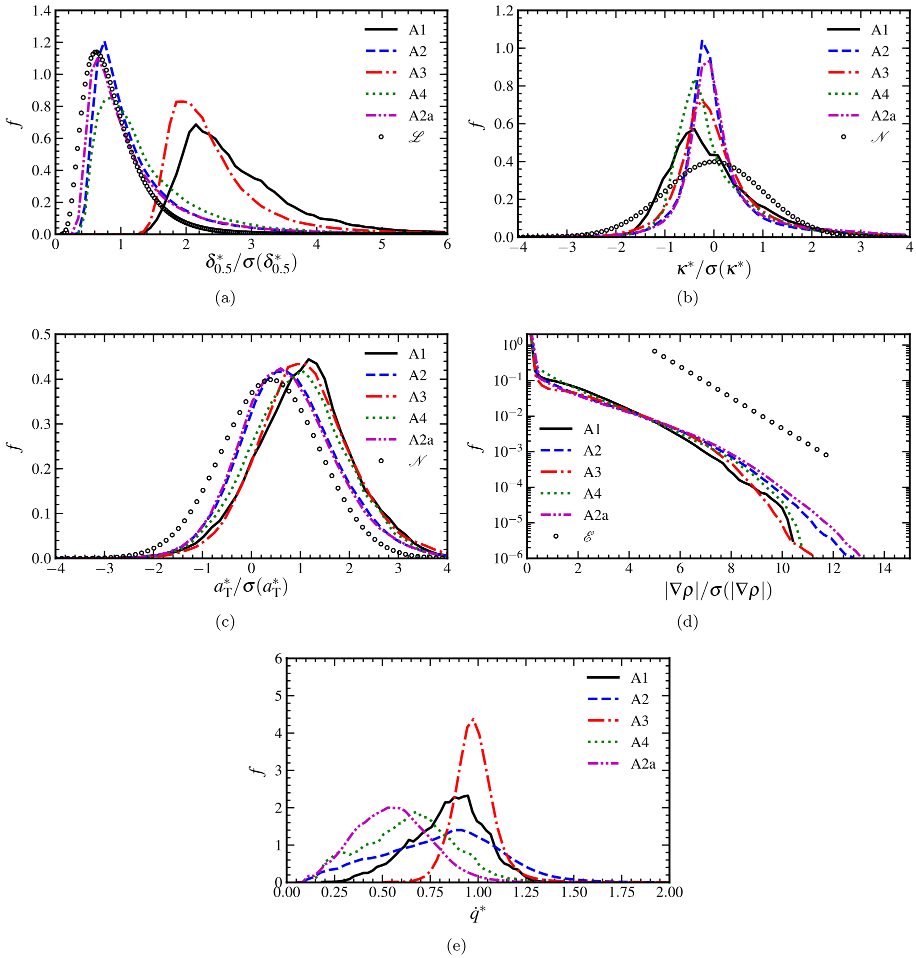

Fig. 8 PDF of the normalized reaction zone thickness (**a**), curvature (**b**), tangential strain rate (**c**), density gradient magnitude (**d**), and heat release rate (**e**). The representative references curves indicated by $\mathcal{L}$, $\mathcal{N}$, and $\mathcal{E}$ denote log-normal, normal, and exponential distributions, respectively

normalized PDF of κ^*, however, there are quantitative differences. The value of μ and σ of κ^* increase while the value of γ decreases in Case A2a compared to Case A2.

The tangential strain rate, a_{T}, affects the flame structure and its propagation characteristics by altering the surface area and the convective transport due to the flow non-uniformity along normal and tangential directions to the flame surface. The heat release within the flame region leads to acceleration of the flow in the flame-normal direction, which induces extensional strain along the tangential direction to the flame surface. Figure 8c shows the PDF of a^*_T, which tends to be positively skewed, thus implying that the extensional strain rate along the flame surface is higher compared to the compressive strain. Such a behavior of turbulent premixed flames is well known (Ashurst 1990; Rutland et al. 1991). In all cases, the mean value is positive (see Table 3). The shape of the PDF of a^*_T can be approximated with a normal distribution in all cases. Even though the extensional strain is dominant, there are events corresponding to the compressive strain with a low to moderate probability. Typically, an extensional (compressive) strain leads to thinning (thickening) of the flame front. However, a net thickening or thinning of the flame front depends upon values of both curvature and tangential strain rate (Peters 2000). The increase in pressure increases the probability of compressive strain, particularly in cases A2 and A4. This can be attributed to enhanced small-scale wrinkling of the flame surface in these cases. Such a behavior is also present in Case A2a, although that can be attributed to a higher *Re* in this case, which also manifests into an enhanced wrinkling of the flame surface.

Figure 8d shows the PDF of the density gradient magnitude $|\nabla \bar{\rho}|$, which is also used to examine the flame structure, as it is associated with the sharpness of the interface of the reactants and products. In all cases, the normalized PDF collapses to an exponential distribution. Such a behavior has been reported in past studies of high *Ka* turbulent premixed flames (Aspden et al. 2011). With an increase in pressure, μ and σ of the normalized density gradient magnitude ($|\nabla \rho| \delta_L/(\rho_b - \rho_b)$) decrease except in Case A4, which is due to the homogenization by the small-scales in these cases. The standard deviation of the normalized density gradient magnitude tends to be sensitive to the changes in the value of u'/S_L and l/δ_L at high pressure, which is associated with the sharpness of the reactants/products interface in these cases. In all cases the PDF tends to be positively skewed, where the skewness tends to increase with *Ka* at a fixed pressure. The decay of the normalized PDF in Case A2a is smaller than in Case A2a, which can be attributed to a higher *Re* in this case that also can enhance the sharpness of the reactants/products interface as evident from Fig. 3.

Figure 8e shows the PDF of $\dot{q}^*$ on the flame surface for all cases. A broader PDF is observed demonstrating the effects of turbulence on heat release. The PDFs also show a noticeable sensitivity to the change in pressure and the characteristic scale ratios. Similar to the past studies of turbulent premixed flames at atmospheric pressure (Tanahashi et al. 2000), a broad PDF of $\dot{q}^*$ occurs in Case A1 with the peak of the PDF occurring closer to the peak value of the heat release rate of the corresponding laminar flame. The PDF is negatively skewed with the mean value of $\dot{q}$ marginally lower than the corresponding laminar flame (see Table 3). The presence of turbulence leads to both higher and lower values of $\dot{q}^*$ compared to its mean. However, no local extinction is evident. The increase of pressure in Case A2 leads to a broadening of the PDF and approach to a nearly symmetric behavior about the peak location, which can be attributed to the fluctuations induced by the increased effect of small-scale eddies. This behavior is much different from that observed in Case A2a where a positively skewed PDF with a much lower mean value is observed. In Case A3, where u'/S_L is reduced compared to Case A2, as expected, the PDF gets narrower and positively skewed with the peak of PDF occurring closer to the peak laminar value. As evident from Table 3, the decrease in u'/S_L leads to a decrease in the standard deviation, which indicates that turbulent eddies, in this case, are not energetic enough to affect the flame structure significantly compared to Case A2. The effect of change in the length scale ratio in Case A4 has a significant effect on the PDF. Although the PDF remains broader as in cases A1 and A2, the location of the peak value of the PDF gets much lower compared to the corresponding peak value of the laminar flame.

The quantitative behavior of the PDFs of the quantities considered here is sensitive to the changes to the characteristics scales of turbulence. However, the normalized PDFs of reaction zone thickness, curvature, tangential strain rate, and density gradient magnitude tend to nearly collapse for the cases matching *Ka* indicating that they tend to be independent of pressure.

4.5 Heat Release Rate on Flame Surface

The curvature of flame fronts and tangential strain rate on the flame surfaces are important parameters in the context of flame-front-based turbulent combustion modeling (Echekki and Chen 1996; Tanahashi et al. 2000; Chakraborty and Cant 2004). Therefore, we examine the relationship of heat release rate with curvature and the tangential strain rate in terms of their joint PDF and conditional variation.

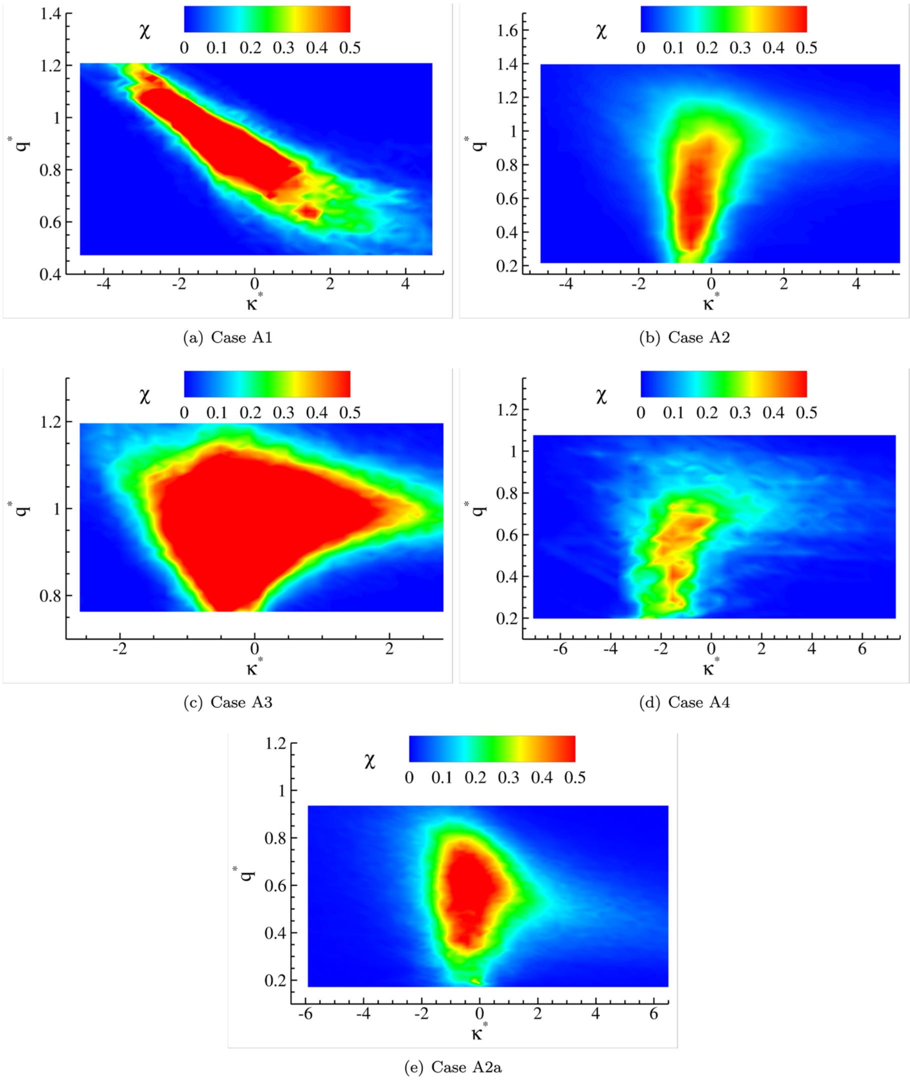

(a) Case A1 (b) Case A2

(c) Case A3 (d) Case A4

(e) Case A2a

Fig. 9 Contours of the joint PDF of heat release rate and curvature for all cases

Figure 9 shows the contours of the joint PDF of $\dot{q}^*$ and κ^*. Qualitatively, the shape of the contours of the joint PDF tends to be significantly affected by pressure. This is also evident quantitatively in terms of the values of the correlation coefficient of $\dot{q}^*$ and κ^*, which are −0.86, 0.03, −0.12, 0.14, -and −0.35 in cases A1, A2, A3, A4, and A2a, respectively. Here, the correlation coefficient is is the normalized covariance of $\dot{q}^*$ and κ^*, where the normalization is based on the standard deviation of $\dot{q}^*$ and κ^*. In particular, in atmospheric pressure flames (cases A1 and A2a), we observe a negative correlation between $\dot{q}^*$ and κ^*. In these cases, the concave flame elements tend to show higher values of $\dot{q}^*$ compared to the convex flame elements. Such a behavior of atmospheric pressure flames is well known, which is indicative of a thermo-diffusively stable flame (Haworth and Poinsot 1992; Rutland and Trouvé 1993; Baum et al. 1994; Tanahashi et al. 2000). However, the behavior is altered in all high-pressure cases, where higher values of $\dot{q}^*$ are usually associated with both positive and negative values of κ^*. Such behavior has also been reported in past studies where heat release rate was observed to enhance at convex regions at high pressure and is indicative of thermo-diffusive instability (Dinesh et al. 2016; Wang et al. 2018, 2019b). Note that $Le < 1$ in all cases (see Fig. 7e), which tends to reduce in high-pressure cases, thus promoting burning in the regions having positive curvature. Specifically, in Case A2, $\dot{q}^*$ and κ^* tend to be highly de-correlated leading to a wide range of values of heat release for flame elements with the same curvature. This can also be attributed to the enhanced small-scale wrinkling as evident in Figs. 2 and 3 in this case. Qualitatively, such behavior is evident in the other two high-pressure cases, albeit with some quantitative differences. In all cases, we can observe the role of turbulence, which causes the presence of both concave and convex flame elements and fluctuations in the value $\dot{q}^*$ of flame elements. As discussed before (see Fig. 8e), cases A1, A2, and A3 show the presence of flame elements with $\dot{q}^* > 1$, which indicates higher values of heat release rate compared to the corresponding laminar flame. This is also evident from the contours of the joint PDF. Although cases A2 and A2a have the same Ka, the effect of pressure is significant on the contours of the joint PDF and the correlation coefficient of $\dot{q}^*$ and κ^*. Another key feature to observe is that the flame elements with $\dot{q}^* > 1$ tend to have primarily negative curvature. This aspect is examined further in terms of conditional variation of $\dot{q}^*$ with κ^*.

Figure 10 shows the conditional variation of $\dot{q}^*$ with respect to κ^*. Similar to the past studies of the atmospheric pressure flames, cases A1 and A2a show a nearly quasi-linear decrease of $\dot{q}^*$ with κ^* (Tanahashi et al. 2000). The flame elements with a higher magnitude of negative κ^* exhibit $\dot{q}^* \gtrapprox 1$, whereas the flame elements with $\kappa^* > 0$ have $\dot{q}^* \lessapprox 1$, particularly in Case A1. As mentioned above, higher values of $\dot{q}^*$ on concave flame elements are indicative of thermo-diffusive stable flame. This behavior is altered in Case A2a due to enhanced effects of turbulent diffusion leading to a weaker burning on concave flame elements. Similar to the joint PDF contours shown in Fig. 9, the variation of $\dot{q}^*$ with κ^* shows significant sensitivity to the increase in pressure. For example in Case A2, the decrease of $\dot{q}^*$ occurs with κ^* on the flame elements having a negative curvature. But compared to cases A1 and A2a, the value of $\dot{q}^*$ tends to be higher in Case A2 for flame elements with the same value of κ^*. Such a behavior has been reported in the past study (Dinesh et al. 2016). A key change occurs to the flame elements with $\kappa^* > 0$, which shows the value of $\dot{q}^*$ similar to a laminar flame unlike in cases A1 and A2a, where $\dot{q}^*$ continuously decreases with an increase in κ^*. In Case A3, a similar variation as Case A2 is observed, although the variation about the mean tends to decrease due to a decrease in u'/S_L in this case. This was also observed in Fig. 8, where compared to Case A2, the PDF of $\dot{q}^*$ tends to be narrower. Furthermore, the conditional variation illustrates that the change in u'/S_L in Case A3 compared to Case A2 does not alter the mean variation of $\dot{q}^*$ with κ^*. However, in Case

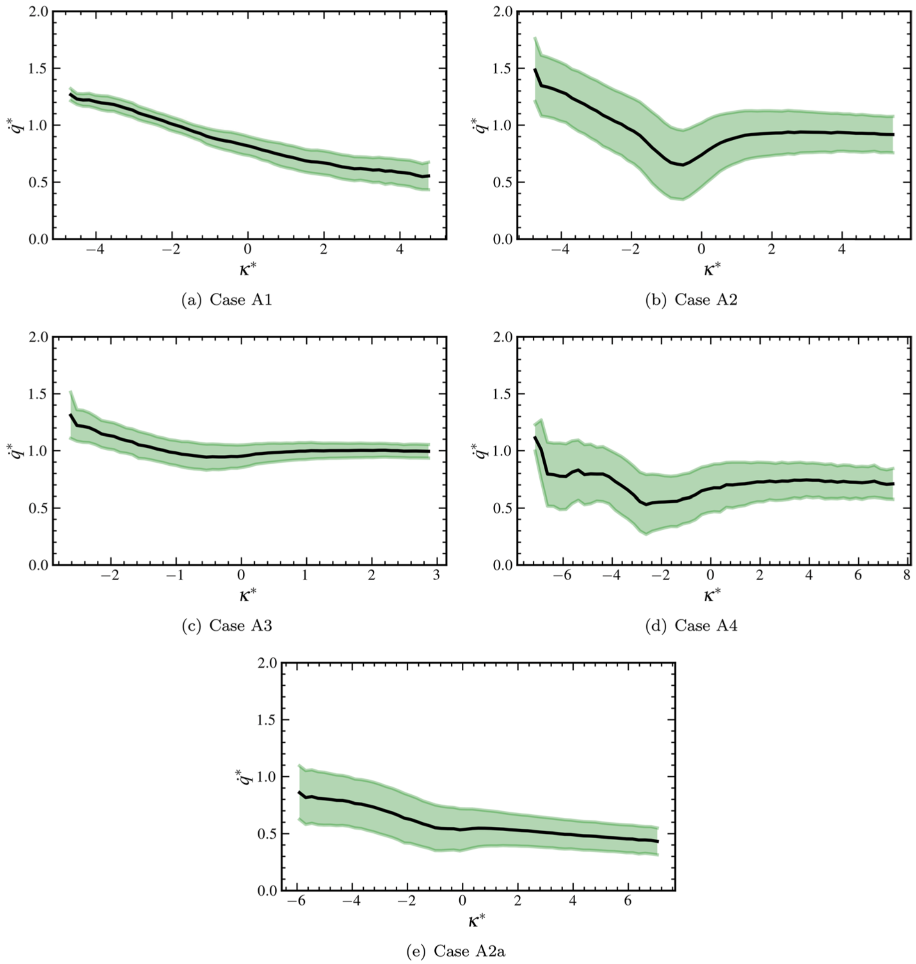

(a) Case A1

(b) Case A2

(c) Case A3

(d) Case A4

(e) Case A2a

Fig. 10 Conditional variation of heat release rate with curvature on the flame surface. The shaded region indicates the standard deviation about the mean variation

A4, although the qualitative variation of $\dot{q}^*$ with respect to κ^* is similar, the flame shows a lower value of $\dot{q}^*$ compared to the corresponding laminar flame. Another key feature to observe is that the standard deviation of $\dot{q}^*$ is the largest in the positive curvature regions and smallest in the negative curvature regions in Case A1. In contrast, the high-pressure cases display the opposite behavior, with standard deviation being the largest and smallest in the negative and positive curvature regions, respectively. This behavior is also observed in Case A2a, which can be attributed to high values of *Re* and *Ka* in this case.

The contours of the joint PDF of $\dot{q}^*$ and a_T^* from all cases are shown in Fig. 11. Similar to the effect of pressure on the joint PDF of $\dot{q}^*$ and κ^*, we observe a noticeable effect on the joint PDF of $\dot{q}^*$ with respect to a_T^*. In particular, we observe a positive correlation between $\dot{q}^*$ and a_T^* in Case A1, which is a well-known feature of atmospheric pressure flames (Tanahashi et al. 2000). The correlation decreases in Case A2a, which can be attributed to the effects of high *Re* and *Ka* in this case, which increases the probability of compressive

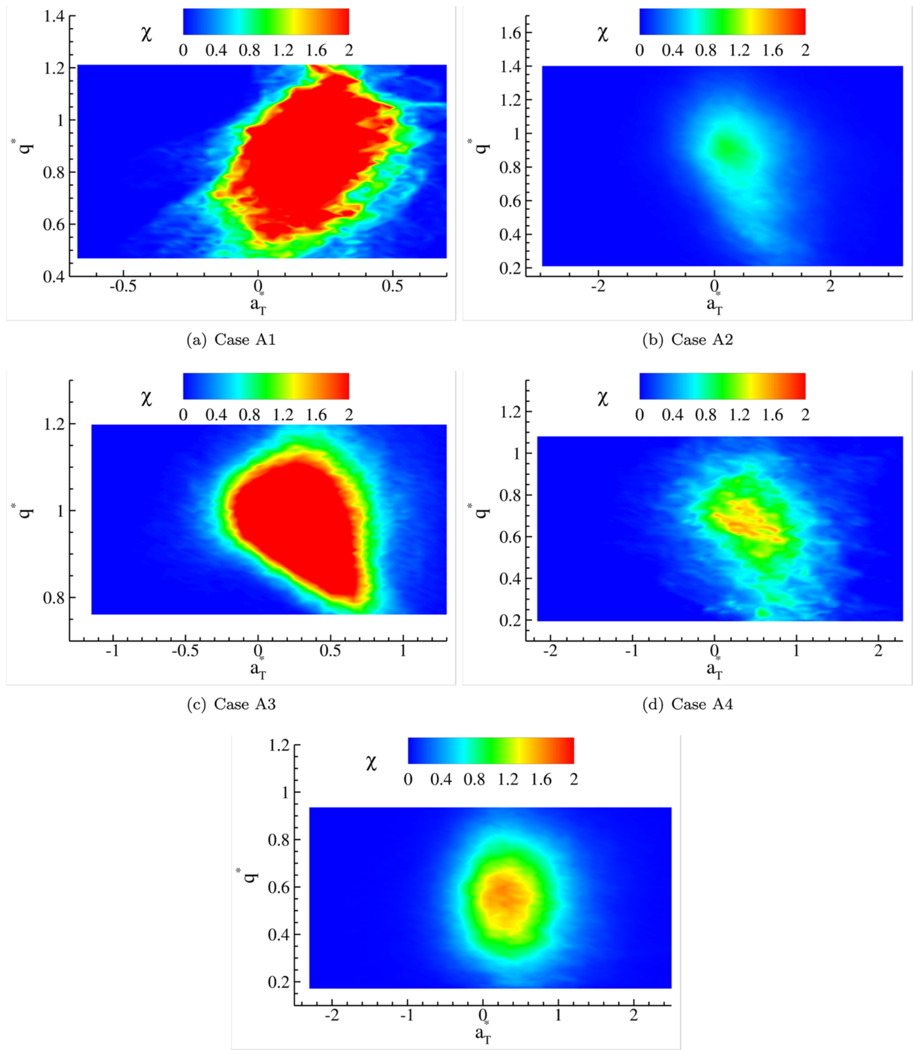

(a) Case A1 (b) Case A2 (c) Case A3 (d) Case A4 (e) Case A2a

Fig. 11 Contours of the joint PDF of the normalized heat release rate and tangential strain rate on the flame surface

strain. However, in all high-pressure cases the correlation between $\dot{q}^*$ and a^*_{T} tends to be negative. In particular, the values of the correlation coefficient between $\dot{q}^*$ and a^*_{T} are 0.34, −0.32, −0.19, −0.24, and −0.03 in cases A1, A2, A3, A4, and A2a, respectively. Regardless of the pressure variation, the flame elements with higher $\dot{q}^*$ tend to be positively stretched ($a^*_{\mathrm{T}} > 0$). Moreover, flame elements with $a^*_{\mathrm{T}} > 0$ tend to be prevalent in all cases. Such a behavior of turbulent premixed flames is well known (Ashurst 1990; Rutland et al. 1991), which is also evident from the statistical measures of a^*_{T} discussed before in Sect. 4.4.

The effects of pressure on the relationship between $\dot{q}^*$ and a^*_{T} can be further inferred from their conditional variation shown in Fig. 12. In Case A1, a positive correlation

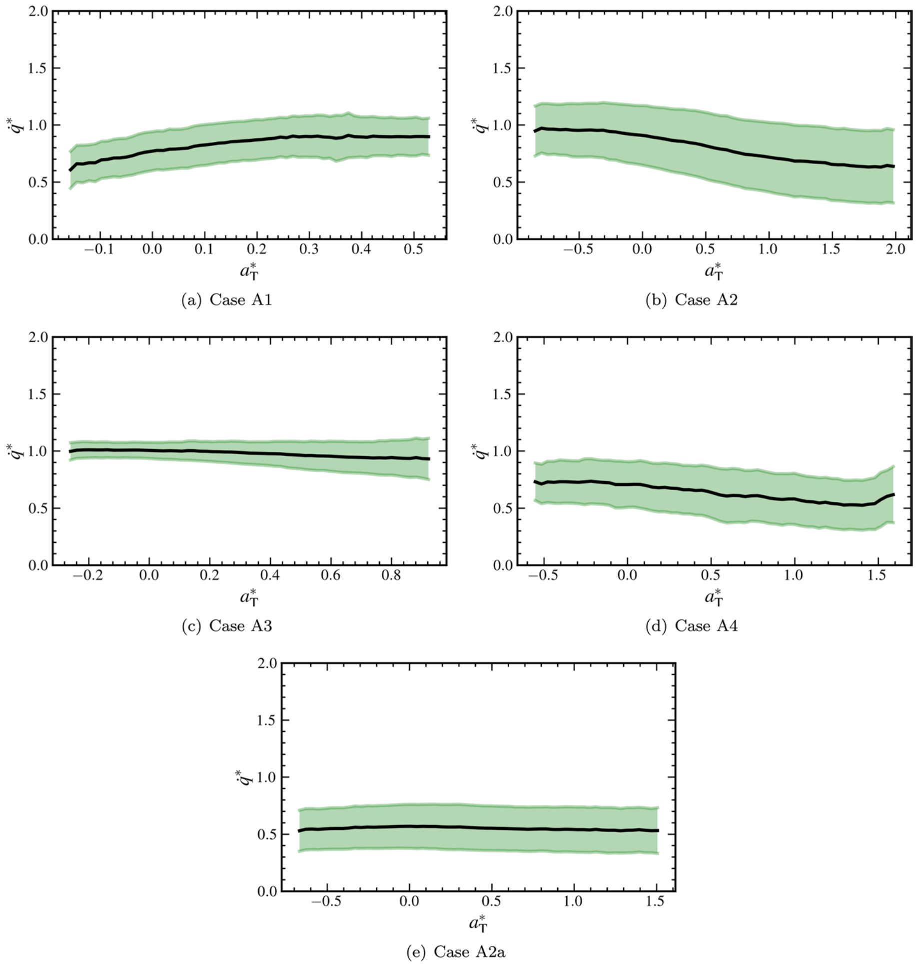

Fig. 12 Conditional variation of heat release rate with tangential strain-rate on the flame surface. The shaded region indicates the standard deviation about the mean variation

between $\dot{q}^*$ and a_T^* yields a gradual increase in $\dot{q}^*$ with a_T^*, which attains a nearly constant value of about 1 with flame elements having very large values of a_T^*. The decrease in correlation between $\dot{q}^*$ and a_T^* in Case A2a leads to nearly constant value of $\dot{q}^*$ with respect to a_T^*. This behavior is altered in high-pressure cases, where $\dot{q}^*$ tends to decrease with a_T^*. In Case A3, $\dot{q}^*$ remains nearly constant with an increase in a_T^*. The behavior of variation about the mean value of $\dot{q}^*$ with respect to a_T^* is also affected by an increase in pressure. While in cases A1 and A2a, the standard deviation of $\dot{q}^*$ tends to be nearly independent of a_T^*, in the high-pressure cases, it tends to increase with a_T^*, which can be attributed to enhanced small-scale wrinkling causing large fluctuations of heat release on flame elements having higher extensional strain rate. The effects of characteristic scale ratios are evident in terms of a higher standard deviation in cases A2 and A4 compared to case A3, which was also observed for the conditional variation of $\dot{q}^*$ with κ^* in Fig. 10, which is due to a lower *Ka* in case A3.

The statistical results discussed in this section demonstrate the effects of pressure and the presence of turbulence and its characteristics on the relationship of the heat release rate with the curvature and the tangential strain rate. In particular, the relationship is significantly affected by an increase in the pressure compared to the effects of the changes to the characteristic scale ratios for the conditions considered in this study. The differences observed in cases A2 and A2a, which have the same *Ka* can be attributed to the nonlinear effects of pressure and *Re* on the heat release rate on different types of flame elements.

5 Conclusions

An improved fundamental understanding of flame-turbulence interactions in turbulent premixed flames under different operating conditions is key to the development of novel and efficient models with predictive capabilities. In this study, the effects of pressure and the characteristics scale ratios (u'/S_L and l/δ_L) at high pressure on the flame-turbulence interactions are examined using DNS of freely propagating lean methane/air turbulent premixed flames. A canonical temporally evolving configuration comprising an initially planar laminar flame interacting with an initially isotropic background turbulence that decays with time is considered. Specifically, five cases are simulated to characterize the effects of an increase in pressure for the same initial values of turbulence intensity (u') and integral length scale (l), a decrease in u'/S_L at high-pressure for the same value of l/δ_L, a decrease in l/δ_L at high-pressure for the same value of u'/S_L, and a difference in pressure for the cases with the same values of u'/S_L and l/δ_L. The present study complements the findings of some of the past studies of high-pressure turbulent premixed flames by focusing on a detailed analysis of methane/air flames corresponding to different regimes and examining the effects of turbulence, pressure, and characteristic scales ratios at high-pressure. The analysis is carried out in terms of a description of structural, spectral, state-space, and statistical features of the flame-turbulence interactions with a particular emphasis on understanding the behavior of heat release rate and its relationship to curvature and tangential strain rate on the flame surface.

All five cases exhibit an increased wrinkling and spatial broadening of the flame brush compared to the corresponding laminar flames. This is due to the wrinkling and stretching of the initially planar flame by the turbulent eddies that induce homogenization by transporting heat and mass away from the heat-release region. A quantitative difference occurs across the five cases demonstrating the effects of pressure and characteristic scale ratios. Specifically, compared to the atmospheric pressure flame at low *Ka*, the wrinkling and the mean flame broadening are enhanced by about 3 and 5.5 times, respectively, with an increase in pressure while having the same initial values of u' and l. This is due to an increase in the range of small-scale energetic eddies at high pressure, which was also evident from the distribution of the spectral kinetic energy. At high pressure, a decrease in u'/S_L leads to a decrease in the broadening and wrinkling of the flame. However, the decrease in l/δ_L showed significant differences compared to the other two high-pressure cases, where the spatial structure approached the atmospheric pressure case even with a high *Ka*. The cases having the same *Ka* and differing in pressure show differences in the amount of wrinkling, flame broadening, and the approach to the post-flame temperature. Although these cases exhibit qualitatively similar structural features of flame, the underlying reasons for enhanced wrinkling and flame broadening are different. For example, while in the high-pressure case, the range of energetic small scales is extended, in the atmospheric pressure flame, the initial *Re* tends to be higher, which apart from affecting the range of scales of motion, also affects their kinetic energy. From the spectral viewpoint, the effects of heat release and the associated thermal expansion led to a dissipation of the small scales on the products side, where again a sensitivity to an increase in the pressure and changes in u'/S_L and l/δ_L was observed.

The spatially-averaged flame structure gets significantly affected due to changes in pressure and characteristic scale ratios at high pressure. In particular, at high pressure, due to enhanced transport, a higher temperature is observed ahead of the mean flame location compared to atmospheric pressure flames. In the post-flame region, the increase in temperature tends to be sharper in high-pressure cases compared to the gradual increase in temperature observed in the atmospheric pressure flames. The spatial variation of mass fraction of species such as CO, CO_2, and H_2 tend to be very sensitive to changes in pressure and the changes in the length scale ratio at high pressure. In particular, the mass fraction of intermediate species such as CO and H_2 reduces significantly in high-pressure flames compared to the atmospheric pressure flames in the post-flame region, which indicates a complete and compact burning at high-pressure. The effect of pressure in cases with the same *Ka* is much more apparent in the variation of the intermediate species, which is due to the differences in the range of scales of motion and the turbulent kinetic energy associated with such scales in these cases.

The state-space variation of temperature with respect to the progress variable showed a quasi-linear variation with only minor sensitivity to pressure and characteristic scale ratios, thus implying that a simpler pressure-dependent low-dimensional manifold representation of such flames can be accomplished. However, the variation of other thermochemical quantities such as heat release rate and mass fraction of the intermediate species (CO and H_2) showed a high degree of sensitivity and highly nonlinear behavior to the effects of pressure, changes to u'/S_L and l/δ_L, and the dominance of turbulent diffusion in high *Ka* cases, thus indicating the need to accurately account for these effects while employing a low-dimensional manifold representation of such flames. In the state space, a local flame thinning is observed in the preheat region of the high-pressure cases, which was also observed in high *Re* atmospheric pressure flame. However, significant differences are observed in the low- and high-pressure cases in the flame and post-flame regions.

Qualitatively, the single-point statistics of reaction zone thickness, tangential strain rate, curvature, and density gradient magnitude showed an approach to log-normal, normal, normal, and exponential distributions, respectively, in a manner similar to the atmospheric pressure flames in the TRZ regime. However, the effects of pressure and the values of l and u' were apparent in the modification of the shape of these PDFs. Specifically, the PDFs demonstrated the competing effects of straining and mixing effects of turbulent eddies, and differential diffusion in the presence of heat release. Contrary to atmospheric pressure flames where an increase in *Ka* leads to the approach of the PDF of curvature to Gaussian, at high pressure, this was not evident in the cases considered here. The increase in pressure also led to an increase in the probability of compressive strain. The cases matching *Ka* demonstrate a near-collapsing behavior of the normalized PDFs, although there are differences in the statistical measures, which can be attributed to a difference of *Re* in these cases. The presence of turbulence led to fluctuations in the heat release rate on the flame surface. However, no local extinction was observed in any of the cases.

Finally, the relationship of the heat release rate with the curvature and the tangential strain rate was examined on the flame surface. The correlation of heat release rate and curvature is significantly affected by pressure, where a negative correlation at atmospheric pressure is altered to a reduced correlation in higher pressure cases. Furthermore, the conditional variation is modified on the flame elements with positive curvature. The sensitivity to u'/S_L and l/δ_L on this variation is relatively smaller compared to the increase in the pressure. Such a significant change in the relationship of the heat release rate with the tangential strain rate at high pressure is also observed where a gradual increase of the heat release rate with the tangential strain rate is changed to a decrease of the heat release rate with the tangential strain rate.

The results in this study demonstrate the highly nonlinear and multi-scale nature of flame-turbulence interactions, which are affected by operating conditions. The spatial, spectral, and statistical features of such interactions are highly sensitive to the increase in pressure and the changes in the characteristics scale ratios at high pressure. While some aspects of the flame-turbulence interactions can be described in terms of the effects of an increase in *Ka*, the effect of an increase in pressure at a fixed *Ka* was also clearly observed, thus demonstrating an added complexity in parametrizing such interactions. These results highlight the need to have an accurate representation of both turbulence and pressure effects for predictive modeling of turbulent premixed flames at high pressure in practical applications. In the future study, we will examine aspects of reliable modeling of such flames.

Appendix A. Assessment of Spatial Order of Accuracy

In the present study, we have employed a formally second-order-accurate spatial discretization scheme (see Sect. 2.2) to save on the computational cost. In the past studies using the AVF-LESLIE solver (Yang et al. 2017a, b), a similar approach was used to examine

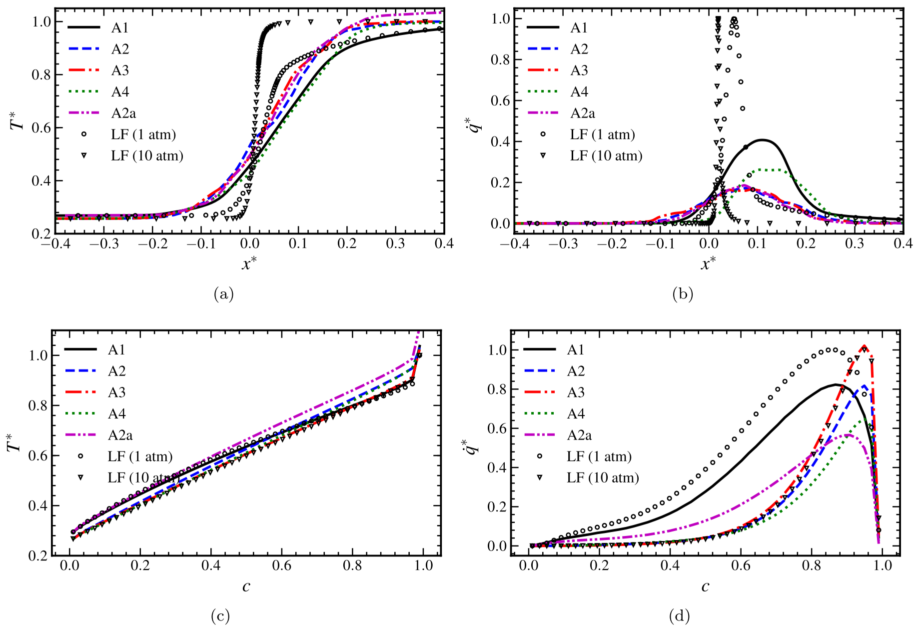

Fig. 13 Spatially (**a**, **b**) and conditionally (**c**, **d**) averaged statistics of normalized temperature (**a**, **c**) and heat release rate (**b**, **d**) for Case A1 at $t/t_0 = 1$

both premixed and non-premixed flames. This is assessed here by comparing the results obtained using second- and fourth-order accurate spatial discretization schemes. These results are shown in Fig. 13 for Case A1, where we compare the spatially and conditionally averaged statistics for Case A1. The approach to obtain spatially- and conditionally-averaged statistics is described in Sects. 4.2 and 4.3, respectively. We can observe that both numerical schemes yield overlapping statistics for temperature and heat release rate fields. The other statistics (not shown here for the sake of brevity) also yield similar results. These results demonstrate the adequacy of the second-order-accurate scheme employed in the present study.

Appendix B. Time Evolution of Statistics

In this study, the structural, spectral, and statistical features of the considered turbulent premixed flames are examined at $t/t_0 = 2$. Note that turbulence decays with time in all cases considered here, however, flame-turbulence interactions attain a nearly quasi-stationary state within one or two eddy-turnover times as discussed in past studies (Savre et al. 2013; Ranjan et al. 2016; Yang et al. 2017a; Nilsson et al. 2018; Panchal et al. 2019). To show that the statistics exhibit nearly similar behavior at different times, we examine the variation of spatially- and conditionally-averaged temperature at $t/t_0 = 2$ and $t/t_0 = 3$, which are shown in Fig. 14 for all cases.

We can observe that the sensitivity of the variation of the normalized temperature along the x-direction to the pressure and the characteristic scales is similar at both times

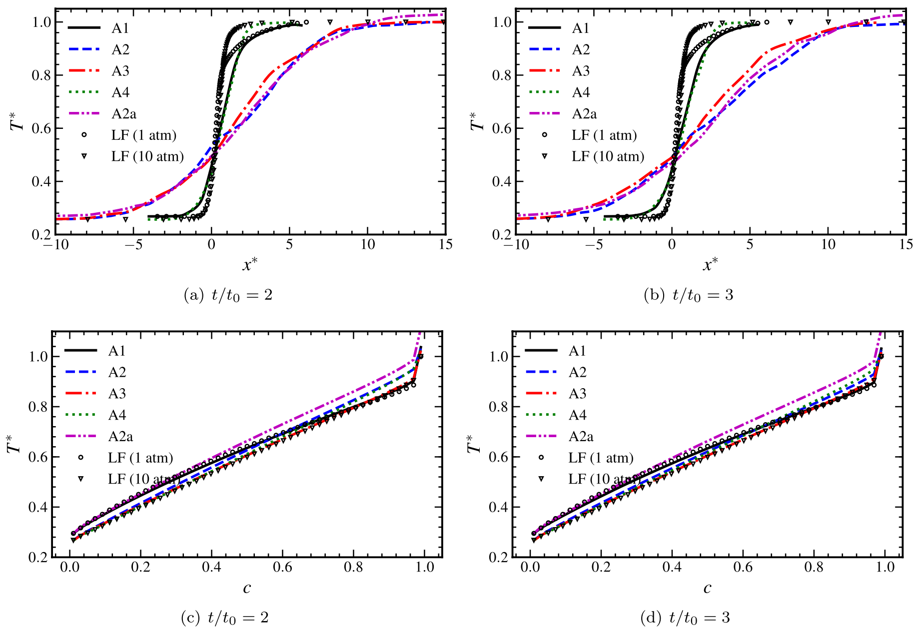

Fig. 14 Spatially (**a**, **b**) and conditionally (**c**, **d**) averaged statistics of normalized temperature (T^*) at $t/t_0 = 2$ and $t/t_0 = 3$

in all cases (see Fig. 14a and b. For example, in the high-pressure cases, particularly, cases A2 and A3, higher values of T^* are observed ahead of the mean flame location ($x^* \approx 0$) compared to the atmospheric pressure flame. The effects of change in pressure between cases A2 and A2a are apparent mainly in the post-flame region, with higher temperatures observed in Case A2a. The effects of change in u'/S_L and l/δ_L are also more evident in the post-flame region. A similar behavior is also observed in the variation of the conditionally averaged temperature field.

It is apparent from Fig. 14c and d that the sensitivity to the changes in pressure and the length-scale and velocity-scale ratios remain similar at $t/t_0 = 2$ and $t/t_0 = 3$. These results indicate that the features of flame-turbulence interactions in different cases can be analyzed at $t/t_0 = 2$.

Acknowledgements This work is supported in part by the Center of Excellence in Applied Computational Science and Engineering (CEACSE) at the University of Tennessee Chattanooga (UTC) and National Science Foundation (NSF) (Grant #: 2301829, Program Officer: Dr. Harsha Chelliah). The computational resources provided by the UTC Research Institute is greatly appreciated.

Author Contributions JB analyzed the results and contributed to writing parts of the manuscript text, ED carried out simulations of this study, and RR provided simulation setup, guided on analysis of the results, and contributed to the manuscript text.

Funding This work is supported in part by CEACSE at the University of Tennessee Chattanooga (UTC) and NSF (Grant #: 2301829, Program Officer: Dr. Harsha Chelliah).

Data Availability The authors can provide access to the datasets used in this study based on an email request to the corresponding author.

Declarations

Conflict of interest The authors have no Conflict of interest to declare.

References

Abdel-Gayed, R., Bradley, D., Hamid, M., Lawes, M.: Lewis number effects on turbulent burning velocity, in: Symposium (international) on combustion, volume 20, Elsevier, pp. 505–512 (1985)

Alqallaf, A., Klein, M., Dopazo, C., Chakraborty, N.: Evolution of Flame Curvature in Turbulent Premixed Bunsen Flames at Different Pressure Levels. Flow Turbulence Combust. **103**, 439–463 (2019)

Ashurst, W.T., Peters, N., Smooke, M.: Numerical simulation of turbulent flame structure with non-unity Lewis number. Combustion science and technology **53**, 339–375 (1987)

Ashurst, W. T.: Pressure influence on the flame front curvature of turbulent premixed flames: comparison between experiment and theory, in: Proceedings of the Summer Program, Center for Turbulence Research, pp. 245–253 (1990)

Aspden, A.J., Day, M.S., Bell, J.B.: Turbulence-flame interactions in lean premixed hydrogen: transition to the distributed burning regime. J. Fluid Mech. **680**, 287–320 (2011)

Bagdanavicius, A., Bowen, P., Syred, N., Crayford, A.: Turbulent flame structure of methane-hydrogen mixtures at elevated temperature and pressure. Combust. Sci. Technol. **185**, 350–361 (2013)

Baum, M., Poinsot, T., Haworth, D., Darabiha, N.: Direct numerical simulation of H2/O2/N2 flames with complex chemistry in two-dimensional turbulent flows. Journal of Fluid Mechanics **281**, 1–32 (1994)

Boger, M., Veynante, D., Boughanem, H., Trouve, A.: Direct numerical simulation analysis of flame surface density concept for large eddy simulation of turbulent premixed combustion. Proc. Combust. Inst. **27**, 917–925 (1998)

Bowers, J., Durant, E., Ranjan, R.: Application of Intrusive and Non-Intrusive Reduced Order Modeling Techniques for Simulation of Turbulent Premixed Flames, in: AIAA Propulsion and Energy 2021 Forum, p. 3634

Bradley, D., Kwa, L., Lau, A., Missaghi, M., Chin, S.: Laminar flamelet modeling of recirculating premixed methane and propane-air combustion. Computers and Fluids **71**, 109–122 (1988)

Carlsson, H., Yu, R., Bai, X.: Direct numerical simulation of lean premixed CH4/air and H2/air flames at high Karlovitz numbers, I. J. of Hydrogen Energy **39**, 20216–20232 (2014)

Cecere, D., Giacomazzi, E., Arcidiacono, N., Picchia, F.: Direct numerical simulation of high pressure turbulent lean premixed CH4/H2-Air slot flames, I. J. of Hydrogen Energy **43**, 5184–5198 (2018)

Chakraborty, N., Cant, S.: Unsteady effects of strain rate and curvature on turbulent premixed flames in an inflow-outflow configuration. Combust. Flame **137**, 129–147 (2004)

Chakraborty, N., Champion, M., Mura, A., Swaminathan, N.: Scalar dissipation rate approach to reaction rate closure, Turbulent premixed flames (2011)

Chen, J.H.: Petascale direct numerical simulation of turbulent combustion-fundamental insights towards predictive models. Proc. Combust. Inst. **33**, 99–123 (2011)

Clavin, P., Williams, F.: Effects of molecular diffusion and of thermal expansion on the structure and dynamics of premixed flames in turbulent flows of large scale and low intensity. J. Fluid Mech. **116**, 251–282 (1982)

Daniele, S., Mantzaras, J., Jansohn, P., Denisov, A., Boulouchos, K.: Flame front/turbulence interaction for syngas fuels in the thin reaction zones regime: turbulent and stretched laminar flame speeds at elevated pressures and temperatures. J. Fluid Mech. **724**, 36–68 (2013)

Day, M.S., Bell, J.B., Bremer, P., Pascucci, V., Beckner, V.E.: Lijewski, Turbulence effects on cellular burning structures in lean premixed hydrogen flames. Combust. Flame **156**, 1035–1045 (2009)

Dinesh, K.R., Shalaby, H., Luo, K., van Oijen, J., Thevenin, D.: Effects of pressure on cellular flame structure of high hydrogen content lean premixed syngas sperical flames: A DNS study, I. J. of Hydrogen Energy **41**, 21516–21531 (2016)

Dinkelacker, F., Manickam, B., Muppala, S.: Modelling and simulation of lean premixed turbulent methane/hydrogen/air flames with an effective Lewis number approach. Combust. Flame **158**, 1742–1749 (2011)

Driscoll, J.F., Chen, J.H., Skiba, A.W., Carter, C.D., Hawkes, E.R., Wang, H.: Premixed flames subjected to extreme turbulence: Some questions and recent answers. Prog. Energy Combust. Sci. **76**, 100802 (2020)

Dunn, M.J., Masri, M.J., Bilger, R.W.: A new piloted premixed jet burner to study strong finite rate chemistry effects. Combust. Flame **151**, 46–60 (2007)

Dunn, M., Masri, A., Bilger, R., Barlow, R., Wang, G.-H.: The compositional structure of highly turbulent piloted premixed flames issuing into a hot coflow. Proc. Combust. Inst. **32**, 1779–1786 (2009)

Echekki, T., Chen, J.H.: Unsteady strain rate and curvature effects in turbulent premixed methane-air flames. Combust. Flame **106**, 184–202 (1996)

Fragner, R., Halter, F., Mazellier, N., Chauveau, C., Gokalp, I.: Investigation of pressure effects on the small scale wrinkling of turbulent premixed Bunsen flames. Proc. Combust. Inst. **35**, 1527–1535 (2015)

De Goey, L., Plessing, T., Hermanns, R., Peters, N.: Analysis of the flame thickness of turbulent flamelets in the thin reaction zones regime. Proc. Combust. Inst. **30**, 859–866 (2005)

Gonzalez-Juez, E.D., Kerstein, A.R., Ranjan, R., Menon, S.: Advances and challenges in modeling high-speed turbulent combustion in propulsion systems. Prog. Energy Combust. Sci. **60**, 26–67 (2017)

Goodwin, D. G., Moffat, H. K., Speth, R. L.: Cantera: An object-oriented software toolkit for chemical kinetics, thermodynamics, and transport processes, http://www.cantera.org, (2014). Version 2.1.2

Hamlington, P.E., Poludnenko, A.Y., Oran, E.S.: Interactions between turbulence and flames in premixed reacting flows. Physics of Fluids **23**, 125111 (2011)

Haworth, D., Poinsot, T.: Numerical simulations of Lewis number effects in turbulent premixed flames. Journal of fluid mechanics **244**, 405–436 (1992)

Ichikawa, A., Naito, Y., Hayakawa, A., Kudo, T., Kobayashi, H.: Burning velocity and flame structure of CH4/NH3/air turbulent premixed flames at high pressure, I. J. of Hydrogen Energy **44**, 6991–6999 (2019)

Inauen, A., Kreutner, W.: Griebel, P., Scharen, R., Siewert, P., Bombach, R. Flow field and structure of turbulent high-pressure premixed methane/air flames, in: Turbo Expo: Power for Land, Sea, and Air **36851**, 301–310 (2003)

Keppeler, R., Tangermann, E., Allaudin, U., Pfitzner, M.: LES of low to high turbulent combustion in an elevated pressure environment. Flow Turbulence Combust. **92**, 767–802 (2014)

Kim, W.-W., Menon, S.: Numerical modeling of turbulent premixed flames in the thin-reaction-zones regime. Combust. Sci. Technol. **160**, 119–150 (2000)

Klein, M., Nachtigal, H., Hansinger, M., Pfitzner, M., Chakraborty, N.: Flame Curvature Distribution in High Pressure Turbulent Bunsen Premixed Flames. Flow Turbulence Combust. **101**, 1173–1187 (2018)

Kobayashi, H., Seyama, K., Hagiwara, H., Ogami, Y.: Burning velocity correlation of methane/air turbulent premixed flames at high pressure and high temperature. Proc. Combust. Inst. **30**, 827–834 (2005)

Kollmann, W., Chen, J. H.: Pocket formation and the flame surface density equation, in: Symposium (International) on Combustion, volume 27, Elsevier, pp. 927–934 (1998)

Kraichnan, R.H.: Diffusion by a random velocity field. Physics of Fluids **13**, 22–31 (1970)

Lachaux, T., Halter, F., Chauveau, C., Gökalp, I., Shepherd, I.G.: Flame front analysis of high-pressure turbulent lean premixed methane-air flames. Proc. Combust. Inst. **30**, 819–826 (2005)

Lapointe, S., Savard, B., Blanquart, G.: Differential diffusion effects, distributed burning, and local extinctions in high Karlovitz premixed flames. Combust. Flame **162**, 3341–3355 (2015)

Liu, C.-C., Shy, S.S., Peng, M.-W., Chiu, C.-W., Dong, Y.-C.: High-pressure burning velocities measurements for centrally-ignited premixed methane/air flames interacting with intense near-isotropic turbulence at constant Reynolds numbers. Combust. Flame **159**, 2608–2619 (2012)

Lowery, C., Hasti, V. R., Ranjan, R.: Characteristics of Non-Equilibrium Turbulence in Couette Flow under Compressible Conditions, in: AIAA AVIATION 2022 Forum, p. 4035

Lu, Z., Yang, Y.: Modeling pressure effects on the turbulent burning velocity for lean hydrogen/air premixed combustion. Proc. Combust. Inst. **000**, 1–8 (2020)

Maas, U., Pope, S.B.: Simplifying chemical kinetics: intrinsic low-dimensional manifolds in composition space. Computers and Fluids **88**, 239–264 (1992)

MacCormack, R.W.: The effect of viscosity in hypervelocity impact cratering. J. Space. Rockets **40**, 757–763 (2003)

Mansour, M.S., Peters, N., Chen, Y.C.: Investigation of local flame structures and statistics in partially premixed turbulent jet flames using simultaneous CH LIF/Rayleigh laser technique. Proc. Combust. Inst. **27**, 767–773 (1998)

Nie, Y., Wang, J., Guo, S., Zhang, W., Jin, W., Zhang, M., Huang, Z.: POD scale analysis of turbulent premixed flame structure at elevated pressures. Combust. Sci. Technol. **193**, 944–966 (2021)

Nilsson, T., Carlsson, H., Yu, R., Bai, X.-S.: Structures of turbulent premixed flames in the high Karlovitz number regime-DNS analysis. Fuel **216**, 627–638 (2018)

Oijen, J., Goey, L.D.: Modelling of premixed laminar flames using flamelet-generated manifolds. Combust. Sci. Technol. **161**, 113–137 (2000)

Panchal, A., Ranjan, R., Menon, S.: A Comparison of Finite-Rate Kinetics and Flamelet-Generated Manifold Using a Multiscale Modeling Framework for Turbulent Premixed Combustion. Combust. Sci. Technol. **191**, 921–955 (2019)

Peters, N.: Turbulent Combustion. University Press, Cambridge Turbulent Combustion (2000)

Poinsot, T., Veynante, D.: Theoretical and Numerical Combustion. Edwards Inc, Theoretical and Numerical Combustion, edition (2005)

Ranjan, R., Muralidharan, B., Nagaoka, Y., Menon, S.: Subgrid-Scale Modeling of Reaction-Diffusion and Scalar Transport in Turbulent Premixed Flames. Combust. Sci. Technol. **188**, 1496–1537 (2016)

Ranjan, R., Menon, S.: Numerical Investigation of Structural and Statistical Features of Premixed Flame under Intense Turbulence, in: International Symposium on Turbulence and Shear Flow Phenomena, volume 10 (2017)

Ratzke, A., Schöffler, T., Kuppa, K., Dinkelacker, F.: Validation of turbulent flame speed models for methane-air-mixtures at high pressure gas engine conditions. Combust. Flame **162**, 2778–2787 (2015)

Rieth, M., Gruber, A., Chen, J.H.: The effect of pressure on lean premixed hydrogen-air flames. Combustion and Flame **250**, 112514 (2023)

Rutland, C., Trouvé, A.: Direct simulations of premixed turbulent flames with nonunity Lewis numbers. Combust. Flame **94**, 41–57 (1993)
Rutland, C.. J., Ferziger, J.. H., El Tahry, S.. H.: Full numerical simulations and modeling of turbulent premixed flames, in: Symposium (International) on Combustion. Elsevier **23**, 621–627 (1991)
Sankaran, R., Hawkes, E.R., Chen, J.H., Lu, T., Law, C.K.: Structure of a spatially developing turbulent lean methane-air Bunsen flame. Proc. Combust. Inst. **31**, 1291–1298 (2007)
Sankaran, V., Menon, S.: Subgrid combustion modeling of 3-D premixed flames in the thin-reaction-zone regime. Proc. Combust. Inst. **30**, 575–582 (2005)
Savard, B., Bobbitt, B., Blanquart, G.: Structure of a high Karlovitz n-C 7 H 16 premixed turbulent flame. Proc. Combust. Inst. **35**, 1377–1384 (2015)
Savard, B., Lapointe, S., Teodorczyk, A.: Numerical investigation of the effect of pressure on heat release rate in iso-octane premixed turbulent flames under conditions relevant to SI engines. Proc. Combust. Inst. **36**, 3543–3549 (2017)
Savre, J., Carlsson, H., Bai, X.S.: Turbulent methane/air premixed flame structure at high Karlovitz numbers. Flow Turbulence Combust. **90**, 325–341 (2013)
Smith, T.M., Menon, S.: One-Dimensional Simulations of Freely Propagating Turbulent Premixed Flames. Combust. Sci. Technol. **128**, 99–130 (1997)
Soika, A., Dinkelacker, F., Leipertz, A.: Pressure influence on the flame front curvature of turbulent premixed flames: comparison between experiment and theory. Combust. Flame **132**, 451–462 (2003)
Srinivasan, S., Menon, S.: Linear Eddy Mixing Model Studies of High Karlovitz Number Turbulent Premixed Flames. Flow Turb. Combust. **93**, 189–219 (2014)
Steinberg, A.M., Hamlington, P.E., Zhao, X.: Structure and dynamics of highly turbulent premixed combustion. Prog. Energy Combust. Sci. **85**, 100900 (2021)
Tanahashi, M., Fujimura, M., Miyauchi, T.: Coherent fine-scale eddies in turbulent premixed flames. Proc. Combust. Inst. **28**, 529–535 (2000)
Towery, C. A. Z., Poludnenko, A. Y., Urzay, J ., O'Brien, J., Ihme, M., Hamilngton, P., Towery, C. A. Z. and Poludnenko, A. Y. and Urzay, J. and O'Brien, J. and Ihme, M. and Hamilngton, P.E.: Spectral Kinetic Energy Transfer in Turbulent Premixed Reacting Flows Phys. Rev. E 93 (2016) 053115
Trouve, A., Poinsot, T.: The evolution equation for the flame surface density in turbulent premixed combustion. J. Fluid Mech. **278**, 1–31 (1994)
Wabel, T.M., Skiba, A.W., Driscoll, J.F.: Turbulent burning velocity measurements: Extended to extreme levels of turbulence. Proc. Combust. Inst. **36**, 1801–1808 (2017)
Wabel, T.M., Skiba, A.W., Temme, J.E., Driscoll, J.F.: Measurements to determine the regimes of premixed flames in extreme turbulence. Proc. Combust. Inst. **36**, 1809–1816 (2017)
Wang, Z., Abraham, J.: Effects of Karlovitz Number on Flame Surface Wrinkling in Turbulent Lean Premixed Methane-Air Flames. Combust. Sci. Technol. **190**, 363–392 (2018)
Wang, J., Guo, S., Zhang, W., Zhang, M., Huang, Z.: Effect of hydrogen ratio on turbulent flame structure of oxyfuel syngas at high pressure up to 1.0 MPa. I. J. of Hydrogen Energy **44**, 11185–11193 (2019a)
Wang, H., Hawkes, E.R., Chen, J.H., Zhou, B., Li, Z., Aldén, M.: Direct numerical simulations of a high Karlovitz number laboratory premixed jet flame-an analysis of flame stretch and flame thickening. J. Fluid Mech. **815**, 511–536 (2017)
Wang, X., Jin, T., Luo, K.H.: Response of heat release to equivalence ratio variations in high Karlovitz premixed H2/air flames at 20 atm, I. J. of Hydrogen Energy **44**, 3195–3207 (2019)
Wang, X., Jin, T., Xie, Y., Luo, K.: Pressure effects on flame structures and chemical pathways for lean premixed turbulent H2/air flames: Three-dimensional DNS studies. Fuel **215**, 320–329 (2018)
Wang, J., Matsuno, F., Okuyama, M., Ogami, Y., Kobayashi, H., Huang, Z.: Flame front characteristics of turbulent premixed flames diluted with CO2 and H2O at high pressure and high temperature. Proc. Combust. Inst. **34**, 1429–1436 (2013)
Wang, J., Yu, S., Zhang, M., Jin, W., Huang, Z., Chen, S., Kobayashi, H.: Burning velocity and statistical flame front structure of turbulent premixed flames at high pressure up to 1.0 MPa. Exp Thermal and Fluid Sci. **68**, 196–204 (2015)
Yang, S., Ranjan, R., Yang, V., Menon, S., Sun, W.: Parallel on-the-fly adaptive kinetics in direct numerical simulation of turbulent premixed flame. Proc. Combust. Inst. **36**, 2025–2032 (2017)
Yang, S., Ranjan, R., Yang, V., Sun, W., Menon, S.: Sensitivity of predictions to chemical kinetics models in a temporally evolving turbulent non-premixed flame. Combust. Flame **183**, 224–241 (2017)
Yenerdag, B., Fukushima, N., Shimura, M., Tanahashi, M., Miyauchi, T.: Turbulence-flame interaction and fractal characteristics of H2-air premixed flame under pressure rising condition. Proc. Combust. Inst. **35**, 1277–1285 (2015)
Yilmaz, B., Gokalp, I.: Analysis of turbulent lean premixed methane-air flame statistics at elevated pressures. Energy Fuels **31**, 12815–12822 (2017)

Yuen, F., Gülder, Ö.L.: Investigation of dynamics of lean turbulent premixed flames by Rayleigh imaging. AIAA J. **47**, 2964–2973 (2009)

Zhang, M., Wang, J., Chang, M., Huang, Z.: Turbulent flame topology and the wrinkled structure characteristics of high pressure syngas flames up to 1.0 MPa. I. J. of Hydrogen Energy **44**, 15973–15984 (2019)

Zhou, B., Brackmann, C., Wang, Z., Li, Z., Richter, M., Aldén, M., Bai, X.-S.: Thin reaction zone and distributed reaction zone regimes in turbulent premixed methane/air flames: Scalar distributions and correlations, Combust. Flame 175 (2017)

Authors and Affiliations

Jamie Bowers[1] · Eli Durant[1] · Reetesh Ranjan[1]

✉ Reetesh Ranjan
reetesh-ranjan@utc.edu

[1] Department of Mechanical Engineering, The University of Tennessee Chattanooga, 615 McCallie Avenue, Chattanooga, TN 37403, USA